AIP | Physics of Fluids

Space-time aspects of a three-dimensional multi-modulated open cavity flow

J. Basley, L. R. Pastur, N. Delprat, and F. Lusseyran

Citation: Phys. Fluids **25**, 064105 (2013); doi: 10.1063/1.4811692
View online: http://dx.doi.org/10.1063/1.4811692
View Table of Contents: http://pof.aip.org/resource/1/PHFLE6/v25/i6
Published by the AIP Publishing LLC.

PHYSICS OF FLUIDS **25**, 064105 (2013)

Space-time aspects of a three-dimensional multi-modulated open cavity flow

J. Basley,[1,2,3] L. R. Pastur,[1,2] N. Delprat,[1,4] and F. Lusseyran[1]
[1]*LIMSI-CNRS, BP 133, F-91403 Orsay Cedex, France*
[2]*Université Paris-Sud, F-91405 Orsay Cedex, France*
[3]*LTRAC, Department of Aerospace and Mechanical Engineering, Monash University, Melbourne, VIC 3800, Australia*
[4]*Université Pierre & Marie Curie, F-75252 Paris Cedex 5, France*

(Received 10 January 2013; accepted 28 May 2013; published online 28 June 2013)

Side-band frequencies in an incompressible flow past a rectangular cavity are characterized through their space-time coherent structures. A parametric study over a range of dimensionless cavity length L/θ_0 has been carried out in the incompressible regime. It yields the general evolution of self-sustained oscillations, for which primary characteristics match results in the literature. The modulating frequencies associated with side-band frequencies are usually imputed either to the two-dimensional (vortex-edge) interaction at the impingement or to three-dimensional dynamics induced by centrifugal instabilities in the inner-flow. However, secondary order features sometimes depart from commonly accepted scheme. In addition to the salient features of the flow, our observations bring to light another modulation, which may be related to the main recirculation inside the cavity. That modulation even becomes predominant for peculiar configurations. The present work focuses on such a configuration with a cavity length/depth ratio $L/D = 1.5$ and dimensionless cavity length $L/\theta_0 = 76$. Based on time-resolved velocity measurements, the extensive analysis is concerned with the non-linear interactions within the flow. Using laser Doppler velocimetry and time-resolved particle image velocimetry in two planes, this multi-modulated regime is so addressed through both local and global aspects. Time-resolved velocity fields provide space-time coherent data that are analysed using transfer functions, space-time diagrams, and space-extended time-Fourier decomposition. © *2013 AIP Publishing LLC*. [http://dx.doi.org/10.1063/1.4811692]

I. INTRODUCTION

Impinging flows have been long studied for their astonishing features and practical applications ranging from woodwind to structure damage or noise generation. While the range of amplified frequencies is wide when the shear-layer is free, as in Miksad,[1,2] stability properties drastically change for impinging shear-layers. In 1953, Powell[3,4] demonstrated that power spectra reorganize around a few narrow-banded peaks, so-called *edge tones* or *locked-on modes*. This is understood as the result of a feedback-loop through pressure that enhances self-sustained oscillations, often referred as Rossiter[5] modes in compressible flows. In the incompressible limit, the pressure feedback becomes instantaneous. As shown by Sarohia,[6] or Rockwell and Naudascher,[7] shear layer frequencies are mainly aligned with curves close to $\frac{n}{2}\frac{U_0}{L}$, $n \in \mathbb{N}$, with L the cavity length and U_0 the incoming flow velocity. Henceforth, Strouhal numbers associated with shear layer modes must be based on L. When dealing with a laminar incoming flow, the selection of locked-on modes highly depends on the dimensionless cavity length L/θ_0, where θ_0 stands for the incoming boundary layer momentum thickness. New insight has been gained since the 1990s by considering the stability properties of a stationary base state, with respect to which spatially structured perturbations may either be amplified or not (Mamum and Tuckerman[8] and Sipp and Lebedev[9]). Nevertheless, beyond the linear stability properties of the base-flow, the actual flow results from the non-linear saturation

and interactions of the growing modes. Experiments confirm such non-linear interactions. From the pioneer experimental investigations on incompressible impinging flows conducted by Rockwell and co-workers[7,10–12] to experiments in the compressible regime, notably in Kegerise *et al.*[13] or Delprat,[14,15] all studies pointed out amplitude modulations (Refs. 12, 14, and 15) or/and mode competition, as detailed in Pastur *et al.*[16] and Lusseyran *et al.*[17] For instance, Rockwell and Knisely[18] reported two main amplitude-modulated regimes in their experiments dealing with an open flow impinging upon an edge. In the first regime, power spectra exhibit a dominant mode f_a, called β in Ref. 18, fundamental frequency of the self-sustained oscillations, together with a sub-harmonic peak at about $f_a/2$. The second regime gives rise to peaks at $0.4f_a$ and $0.6f_a$, related to a low-frequency modulation of mode f_a by $0.4f_a$. More peaks at $0.2f_a$ and $0.8f_a$ are encountered in a similar configuration in Ref. 12. More generally, the most salient amplitude modulations to be reported in the literature are related to two-dimensional vortex-edge interactions at the impingement. The dominant frequency f_a can be seen as a *carrier* modulated by a low frequency, referred to as the *edge frequency* f_b in the following. The edge frequency typically corresponds to Strouhal numbers based on cavity length L, such that $0.25 \leq f_b L/U_0 \leq 0.4$. We have recovered the above mentioned features in an experimental parametric study, varying both Reynolds number and cavity aspect ratio, in the incompressible regime.

For compressible flows, Delprat[14,15] analysed a wide number of experimental results and proposed a new model interpreting the Rossiter equation as the result of amplitude modulations of the self-sustained oscillations by low frequencies. Since then, Malone *et al.*[19] applied extensively this model to identify the spectral components issued of experimental results at subsonic Mach numbers. In the present study, the non-linear interactions are also characterized as amplitude modulations and then physically interpreted in terms of coherent structures.

Another type of modulation by far smaller frequencies has also been observed in cavity-flow configurations and is generally imputed to spanwise structures (Rockwell and Knisely[20] and Koseff and Street[21]). For instance, Neary and Stephanoff[22] published in 1987 experimental results in which a regime was showing a side-band peak, located at $f_2 \simeq 0.9f_1$, with f_1 the dominant peak (corresponding to f_a in the present study). They related appearance of that side-band peak to a spanwise modulation of cavity main recirculation by a low frequency $f_1 - f_2$. In lid-driven cavity flows, many studies have been carried out to bring to light spanwise distributed vortical structures winding onto the main recirculation (Albensoeder *et al.*,[23–25] Guermond *et al.*,[26] and Migeon *et al.*[27]). Only recently experimental works by Faure *et al.*[28,29] have recognized similar vortical structures in open cavity flows. Mainly based on smoke visualizations, Faure *et al.*[28] were able to characterize the three-dimensional coherent structures of the inner-flow in terms of Görtler instabilities. Such features are responsible for frequencies one order smaller than those corresponding to shear layer modes. Meanwhile, three-dimensional (global) linear instabilities have been intensively studied numerically over the past ten years, notably in cavity flows. See for instance Theofilis[30] and Theofilis and Colonius,[31] or more recently Vicente *et al.*[32,33] and Meseguer-Garrido *et al.*[34] In particular, Brès and Colonius[35] used both linear stability analysis and direct numerical simulations to characterize centrifugal instabilities arising in the inner cavity flow in the compressible regime. They have shown that these centrifugal instabilities organize themselves as spanwise waves whose wavenumbers scale on cavity depth D almost regardless of Mach number and fairly match experimental results cited above. Frequencies associated with resulting spanwise structures also scale on D such that $0.011 \leq \mathrm{St}^D = fD/U_0 \leq 0.026$. Among other parameters, Strouhal numbers actually depend on cavity aspect ratio and dimensionless cavity length L/θ_0. When applied to the frequency gap $f_1 - f_2$ observed by Neary and Stephanoff,[22] the Strouhal number based on D is $\mathrm{St}^D_{1-2} = (f_1 - f_2)D/U_0 = 0.023$, which is consistent with a spanwise modulation process, such as seen in Ref. 35.

There are peculiar configurations for which the frequency distributions seem to be due neither to the two-dimensional effects of the impingement nor to spanwise waves modulating the internal flow. This is, for instance, illustrated in Figure 4 of Rockwell and Naudascher,[11] where some shear-layer frequency peaks do not pertain to the generic scheme of the locked-on modes, although such a scatter was not noted at the time. Likewise, the spectral distributions obtained out of numerical simulations in Gloerfelt[36] focused on the Rossiter[5] modes but showed unexplained secondary order peaks. We have encountered similar regimes exhibiting unexpected frequencies for some restricted

values of the control parameters. Spectra of two of those cases can be seen in Figures 5(b) and 5(c) of Basley *et al.*[37] or in Basley.[38] The spectral distributions are more complex than expected, since a third amplitude modulation of the self-sustained shear layer oscillations may be identified. To our knowledge, the occurrence of such unusual spectral components had only been discussed on a few occasions for compressible flows, see Refs. 13–15. The focus of the present work is to investigate thoroughly the nature of every non-linear interaction in the so-called multi-modulated regimes. One case is studied as a sample of such configurations ($U_0 = 2.1$ m/s, $L/D = 1.5$, $L/\theta_0 = 76$).

In order to better characterize the coherent structures within the flow, we make great use of time-resolved data, which gives access to space-time correlations across the entire region of interest. The experimental facility and data processing methods are first described in Sec. II. Then, Sec. III presents the context of the study. The parametric study, from which the present case is extracted, is briefly reviewed (Sec. III A). A description of the statistical properties of the flow follows (Sec. III B). The spectral signature of the flow is investigated in Sec. IV. Main frequencies are identified in spectra from both laser Doppler velocimetry (LDV) and time-resolved Particle Image Velocimetry (PIV) time-series (Sec. IV A). Time-series and spectrograms (Sec. IV B) provide more insight concerning the possible intermittency of dominant frequencies and non-linear interactions. Section V deals with space-time aspects of the self-sustained oscillations of the shear layer. In the first part, wave properties of the shear layer modes are obtained through estimated transfer functions (Sec. V A). The second part aims to identify coherent structures throughout the space-time domain (Sec. V B) revealing low frequency interactions between the shear layer and the inner-flow main recirculation. Coherent structures are also sought by using modal decomposition, i.e., identifying the spatial modes associated with each relevant time-scale. This is achieved in Sec. VI using *global Fourier* modes, as seen in Rowley *et al.*,[39] Basley *et al.*,[37] and Basley.[38] Fourier decomposition is applied to both cross-stream (xy) and spanwise (xz) planes. Shear layer modes are identified first (Sec. VI A) and spatial structures associated with low frequencies are then discussed in detail (Sec. VI C). Concluding remarks can be read in Sec. VII.

II. EXPERIMENTS AND DATA PROCESSING

A. Wind tunnel facility

The open cavity used in the study is parallelepipedic of depth $D = 50$ mm and span $S = 300$ mm. The cavity length L can be changed from 0 to 100 mm by a sliding backward step. Cavity walls, 2 mm thick, are made of anti-reflection coated glass. The spanwise aspect ratio S/D primarily conveys the influence of spanwise confinement. In the present case, $S/D = 6$ is large enough to consider the effect of lateral walls as a secondary flow, as opposed to fully three-dimensional geometries.[40–42] Coordinate system origin is set mid-span at the upstream edge of the cavity. The x-axis is streamwise, y-axis is normal to the upstream wall along the boundary layer, and z-axis is along the cavity span. The cavity scheme is shown in Fig. 1(a). Incoming flow external velocity U_0 and boundary momentum thickness θ_0 are measured at the leading edge of the cavity, $x = 0$.

The airflow is generated by a centrifugal fan placed upstream of a settling chamber, see Fig. 1(a). Seeding particles (DEHS mineral oil droplets) are injected at the fan inlet. An axial duct, ending with a honeycomb and a contraction, drives the flow towards the test section. In order to produce an established laminar boundary layer at the cavity upstream edge, a flat plate, beginning with an elliptical leading edge that fixes the boundary layer origin, is set at the inlet of the test section. The cavity is inserted into the test facility at a distance $A = 300$ mm from the plate leading edge. The flow is incompressible with a maximum Mach number lower than 0.01. The outlet flow is rejected in the experimental room. It has been checked that the test section upper wall, located at $F = 75$ mm above the cavity, has negligible influence on the development of the boundary layer.

B. LDV measurements

Local streamwise velocity measurements, based on LDV, have been done in the shear layer, 5 mm upstream of the trailing corner, above the cavity top plane: $\{x_{\mathrm{LDV}} = L - 5\ \mathrm{mm}\ , y_{\mathrm{LDV}} = 0.1\,D\}$.

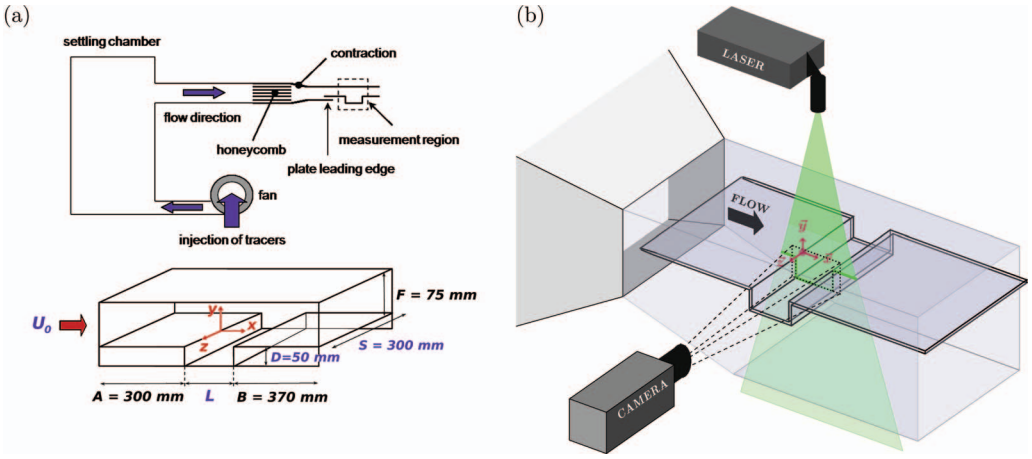

FIG. 1. (a) Wind-tunnel facility with the cavity section in close-up. (b) High-speed PIV setup.

The light source is a continuous argon-ion laser (power 1 W, wavelength 488 nm). The beam is split into two coherent beams by a beam splitter. They cross each other at the LDV point with an angle $\theta = 9^\circ$, generating an interference pattern of interfringe $d = 3.11$ μm. The measuring volume is 1.3 mm in length and 0.1 mm in diameter. One of the two beams travels through a Bragg cell where it is frequency shifted to reduce fringe bias and get rid of direction ambiguity. The first diffracted beam is frequency modulated at $\Delta f = 40$ MHz. Consequently, the interference fringes scroll at velocity $V = d\Delta f \simeq 120$ m/s, such that V is opposite to the inflow velocity. A convergent lens-photomultiplier system is focused on the LDV control volume and detects the intensity variation of the light diffused by the seeding particles passing through the interference pattern. Photomultiplier signal is processed by a Doppler signal analyzer, and the digitized data are stored on a personal computer (PC). For each working point (L/D, U_0), four different LDV measurements were performed, each over a total duration time of about 3 min.

C. High-speed PIV measurements in a cross-stream plane

Planar PIV measurements were conducted at high repetition rate in a xy-plane (cross-stream), providing thereby time-resolved two-dimensional-two-component (2D-2C) velocity fields. The laser sheet was set up at the spanwise position $z/D = 0.4$, such as to avoid symmetry planes of the flow, Fig. 1(b). Light source is delivered by a new wave Pegasus laser. The Pegasus is a dual-head, high repetition rate, diode-pumped Nd:YLF laser system designed for high-speed PIV. The laser is rated at about 10 mJ/pulse at 1 kHz, at wavelength 527 nm (green). Energy is optimal at 1 kHz. Each laser head can operate from 1 to 10 000 pulses/s allowing camera frame rates up to 20 000 frames/s. Each head can be triggered independently. According to the technical sheet, at 1 kHz, the pulse duration is less than 180 ns. Beam diameter is 1.5 mm and divergence is less than 3 mrad.

Image acquisition is performed by a CMOS Photron FASTCAM camera (17×17 μm^2) associated with a 60 mm Micro-Nikkor lens. Using a repetition rate of 1 kHz, it is possible to resolve up to the fifth harmonic of a fundamental shear layer oscillation occurring at up to 100 Hz, which would be enough in our experiments to prevent spectral aliasing. The Photron camera allows us to define two times. The basic time fixes the δt between two shots, from which the velocity field will be computed. The second time Δt, which must be a multiple value of δt (1, 2, 4, 8, 16, 32 times), will provide the time lag between two successive velocity fields. To get optimal light energy, the Pegasus laser flashes at 1 kHz. Our Photron inboard RAM is 2.6 Gb. Gray levels are encoded over 10 bits but stored over 8 bits, which means that the full resolution 1060×640, at repetition time of 1 kHz, acquisition would only last 4 s. A compromise must be found between the basic repetition time and spatial resolution on one hand, and the total acquisition time on another hand.

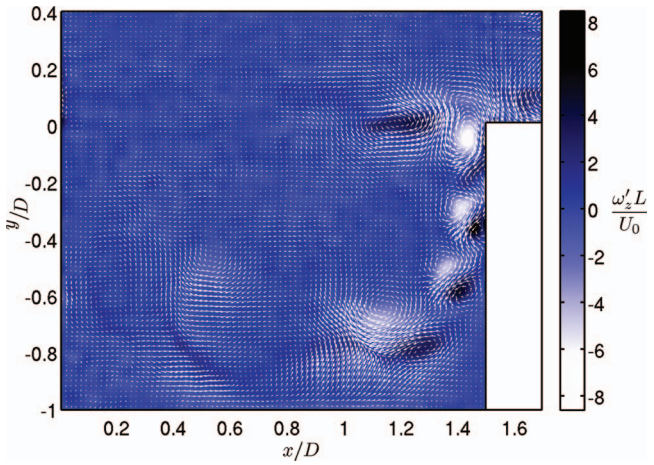

FIG. 2. A snapshot for TR-PIV data, in a cross-stream plane (x, y), for the case $L/\theta_0 = 76$. Colors scale dimensionless vorticity fluctuations $\frac{\omega_z' L}{U_0}$ and vector field represents velocity fluctuations.

To achieve this compromise, the spatial resolution has been reduced to 512 × 400 pixels, allowing 10 484 frames in each 2.6 Gb recording. The PIV acquisition has been conducted at a sampling frequency $f_{frames} = 500$ Hz to get a PIV time delay small enough ($\delta t = 2$ ms), while providing a total acquisition time of 21 s. Note also that using only the central part of the CMOS array – a surface smaller than 9×7 mm^2 – makes parallax distortions almost completely avoided. The time step between velocity fields is set to $\Delta t = 2\delta t = 4$ ms. Time-series sampling frequency is therefore $f_{field} = 250$ Hz. That implies a Nyquist frequency at 125 Hz, which is large enough to prevent spectral aliasing. Indeed, shear-layer oscillation frequency is about 25 Hz and produces three harmonics at the most. Each dataset is hence composed of 5242 velocity fields, computed over a cropped domain of 480 × 400 pixels, for $0 \leq x/D \leq 1.68$ and $-1 \leq y/D \leq 0.4$. A snapshot out of a Time-Resolved PIV (TR-PIV) series is shown in Fig. 2.

Fifteen independent records are performed in the very same conditions to improve the statistical convergence of low-frequency phenomena. Composing a set of 15 time-series makes an overall acquisition time of about 300 s.

D. Standard PIV measurements in a spanwise plane

Dealing with three-dimensional dynamics inside the cavity requires the acquisition of velocity fields in a spanwise plane. Such PIV measurements have been realized to obtain synchronized to LDV measurements: series of 600 velocity fields were acquired (components v_x and v_z) in a zx-plane (parallel to the bottom of the cavity) located at $y/D = -0.34$. The light source is a Quantel laser of 200 mJ at 532 nm. The time duration between two particle images of a single pair was set to 5 ms and the sampling rate at $f_{xz} = 12.5$ Hz. With these characteristics, the datasets are time-resolved with regard to time scales of the spanwise dynamics, but aliasing will occur for shear layer modes.

E. Optical flow

Displacement fields are computed, from particle images, using an optical flow algorithm based on an orthogonal dynamical programming. That algorithm has been detailed in Quénot *et al.*[43] and Basley.[38] Characterization and comparison with various cross-correlation codes are provided in Stanislas *et al.*[44,45] Considering successive stripes out of the particle images, the local displacement $\delta_r^\star(r)$ along the stripe $\mathcal{D}$ is estimated by minimizing the norm of the gray level difference between

the two images (Eq. (1)):

$$\delta_r^\star(r) = \left\{ \delta r \in \mathcal{D} \mid \min_{\delta r} \| I(r + \delta r, t + \delta t) - I(r, t) \| \right\}. \quad (1)$$

This process is performed iteratively on horizontal (vertical) stripes of decreasing height (width), each new iteration using the previous estimation as an initial condition. The calculation ends up with the 2D-2C velocity field at any pixel.

III. CAVITY FLOW AND CONTEXT

A. Overview and parametric study

We have collected the results of several experimental campaigns, based on LDV measurements to illustrate the main spectral features of open cavity flows in the incompressible limit, for aspect ratios between 1 and 2. They are synthesized in Fig. 3, where frequencies of the most energetic modes in power spectra are plotted with respect to the dimensionless cavity length, L/θ_0. Depending on the configuration, spectra exhibit harmonic families and side-band components. Harmonic families correspond in fact to the non-linear saturation of a *carrier* frequency (in black in Fig. 3), representative of self-sustained oscillations. On the other hand, *side-band* frequencies (in gray in Fig. 3) do not produce any harmonics. The frequency distribution shown in Fig. 3 is in good agreement with experimental data obtained by Sarohia[6] and other pioneer works (Refs. 7, 10–12), see for instance Figures 8(b) and 9 in Rockwell and Naudascher.[7] Similarities are also found with various impinging shear flows, as in Figure 4 of Knisely and Rockwell.[12] Most L-based Strouhal numbers align with lines of *locked-on* modes such that

$$\mathrm{St}_n^L \left(\frac{L}{\theta_0} \right) = \frac{f_n L}{U_0} = \frac{n - \gamma_n (L/\theta_0)}{2}, \quad (2)$$

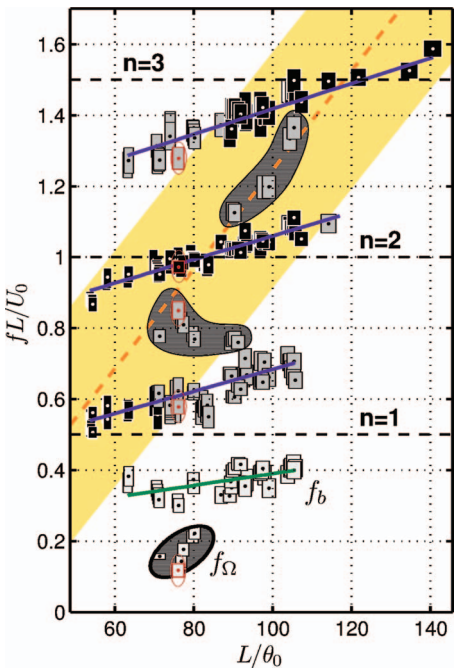

FIG. 3. Primary Strouhal numbers based on L are displayed as functions of dimensionless cavity length L/θ_0; self-sustained oscillations frequencies (black), side-band peaks (gray), and low frequencies (white). Rectangle dimensions represent uncertainties. The shaded area (yellow) is drawn *a posteriori* such as to segregate self-sustained oscillation frequencies from most side-band peaks. It is delimited by $\mathrm{St}^L = \mathrm{St}_*^L \pm 1/3$, with $\mathrm{St}_*^L = 0.014 \times (L/\theta_0 - 10)$ the centerline Strouhal number. Hatched regions highlight side-band frequencies departing from the general scheme.

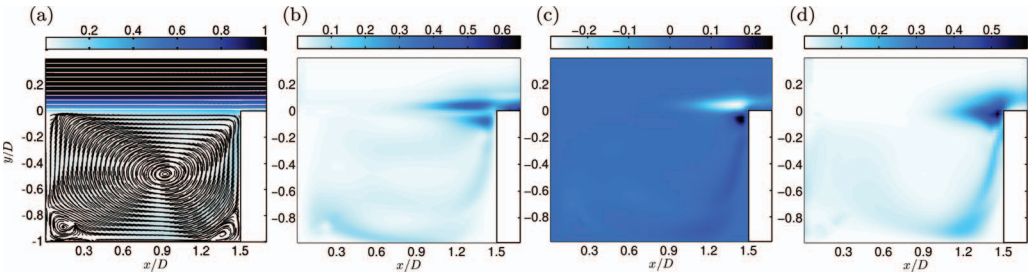

FIG. 4. (a) Mean velocity streamlines colored by normalized mean velocity modulus $|\overline{U}|/U_0$. Normalized Reynolds tensor components (in %). (b) u'^2/U_0^2, (c) $u'v'/U_0^2$, (d) v'^2/U_0^2.

where the parameter $n = 1, 2, 3$ can be seen as the number of cycles within the cavity length: the phase difference between leading and trailing edges is about $2\pi n$. The corrective term γ_n corresponds to the deviation from this ideal phase difference. Such a spectral signature, driven by the dimensionless cavity length, L/θ_0, depicts the dual interaction of both separation/impingement phase relationship and shear layer instability. Oscillating regimes (n) are selected or not, according to their amplification by the shear layer. When two regimes of self-sustained oscillations are equally amplified, two carrier frequencies are selected and *mode switching* occurs, as in Refs. 13, 16, 17, and 46. In order to describe the enhancement of self-sustained oscillations by the intrinsic instability of the impinging shear layer, a parametric domain can be obtained *a posteriori* so that it encompasses all carrier frequencies of self-sustained oscillations and lets aside the side-band frequencies. That domain is depicted in Fig. 3 (shaded region), such that carrier frequencies satisfy

$$|\mathrm{St}_n^L - \mathrm{St}_*^L| \leq 1/3, \tag{3}$$

where the centerline frequency f_* is empirically identified as an affine law

$$\mathrm{St}_*^L\left(\frac{L}{\theta_0}\right) = \frac{f_* L}{U_0} = 0.014 \times \left(\frac{L}{\theta_0} - 10\right). \tag{4}$$

The frequency f_* seems to promote the regime of self-sustained oscillations by enhancing the closest branch n. That could logically imply that f_* is actually close to the most destabilizing frequency of the shear layer.

Each side-band peak denotes amplitude modulation by a low frequency f_b, referred to as the *edge* frequency. By definition, this modulating frequency is always equal to the difference between carrier and side-band frequencies, as seen in Fig. 3. The associated Strouhal number is schematically constant throughout parameter space, approximately around $\mathrm{St}_b^L \simeq 0.35$, increasing only slightly with L/θ_0. On the other hand, remark that ratios f_b/f_a can thus range from 0.25 to 0.65 depending on L/θ_0 and the selected regime of oscillation n.

Some side-band peaks depart from the general scheme of impinging flows: they do not line up with most locked-on modes. Such frequencies are recovered, with some variability, at the same quite unusual location when experiments are reproduced. Hatched areas in Fig. 3 mark off the parametric regions comprising these frequencies. Very similar dispersion could already be observed in Rockwell,[10] for instance, in Fig. 7 of this reference for $1.5 \leq L/D \leq 2$, or in Gloerfelt.[36] However, that gap was not highlighted at the time.

In the forthcoming part of the paper, space and time-resolved data are used to investigate one case among these unusual regimes. That case – observed such that $L/D = 1.5$, $L/\theta_0 = 76$ – exhibits Strouhal numbers that are circled in Fig. 3 (red).

B. Case under study: Statistics

A preliminary study of the flow under investigation is provided by statistics and inviscid linear stability properties obtained from the main PIV dataset. Using high-rate time-resolved PIV, each

TABLE I. Dimensionless parameters with uncertainties.

U_0(m/s)	L/D	L/θ_0	Re_{θ_0}	Re_L
2.10	1.50	76	134	10 200
±1.1%	±0.8%	±1.8%	±2.9%	±1.8%

PIV record is made of 2D-2C velocity fields:

$$\mathbf{U}(\mathbf{r}, t_k) = U_x(x, y, t_k)\mathbf{e}_x + U_y(x, y, t_k)\mathbf{e}_y, \tag{5}$$

where instant $t_k = k\Delta t$ is associated with kth snapshot. With 15 independent PIV records, the entire dataset $\mathbf{U}$ consists of 78 630 fields and provides the time-averaged mean field $\overline{\mathbf{U}}$ and the fluctuation field $\mathbf{u}'$ (Eqs. (6) and (7)). The mean field is shown in Fig. 4(a), where $U_0 = 2.10$ m/s. Streamlines demonstrate the parallel incoming flow and show the main recirculation inside the cavity, centered on about $x/D = 1$:

$$\overline{\mathbf{U}}(\mathbf{r}) = \overline{U}_x(x, y)\mathbf{e}_x + \overline{U}_y(x, y)\mathbf{e}_y, \tag{6}$$

$$\mathbf{u}'(\mathbf{r}, t) = \mathbf{U}(\mathbf{r}, t) - \overline{\mathbf{U}}(\mathbf{r}) = u'(x, y, t)\mathbf{e}_x + v'(x, y, t)\mathbf{e}_y. \tag{7}$$

Incoming boundary layer characteristics are directly measured from streamwise mean-velocity profile $\overline{U}_x(0, y)$, at the cavity inlet $x = 0$, providing displacement and momentum thicknesses $\tilde{\delta}_0^\star = 2.54$ mm and $\tilde{\theta}_0 = 1.10$ mm, respectively. The ratio $h = \tilde{\delta}_0^\star/\tilde{\theta}_0 = 2.32$ indicates that the boundary layer is approximately laminar, allowing to fit the boundary layer profile with a Blasius law; $\mathcal{L}_2$-norm difference between fit and measured profile is indeed about 0.9%. From the fit, the dimensionless cavity length $L/\theta_0 = 76 \pm 1.8\%$ is estimated, as well as the local Reynolds number, based on θ_0. The cavity flow characteristics are provided in Table I.

Normalized Reynolds stresses are presented in Figs. 4(b)–4(d). As expected, Reynolds tensor components $\overline{u'u'}$, $\overline{v'v'}$, $\overline{u'v'}$ show that most of the fluctuating energy is concentrated in the impinging shear layer near the cavity trailing edge. Indeed, the shear layer flapping motion is the most energetic phenomenon in the flow. In particular, $\overline{u'u'}$ – in Fig. 4(b) – exhibits a structure in two lobes distributed on both sides of the cavity top plane ($y = 0$), while $\overline{v'v'}$ – Fig. 4(d) – has a gaussian-like shape centered on $y = 0$. Similar distribution was observed by Refs. 41, 47, and 48. The structure in $\overline{u'v'}$ shows that u' and v' are, in average, of opposite signs atop, and of the same sign below the cavity top-plane. This likely indicates the segregation of traveling vortices at the impingement. More precisely, impinging vortices yielding negative vorticity $\omega_z < 0$ – thus corresponding to $u'(y > 0) > 0$ and $u'(y < 0) < 0$ – dive into the cavity, hence inducing a higher inflow velocity along the wall, that is, $v' < 0$. On the other hand, positive vortices ($\omega_z > 0$) – in other words $u'(y > 0) < 0$ and $u'(y < 0) > 0$ – are "pushed upwards" at the trailing edge to be advected downstream in the wake. Henceforth, one may assume that the flapping motion is responsible for a fluid exchange between inner-flow and outflow at the impingement. Negative vortices gathering vorticity from the incoming boundary layer carry some outflow into the cavity, while positive vortices, yielding a lack of vorticity in the shear layer, can catch some fluid from the main recirculation and bring it up out. Some fluctuations of secondary order are also observed inside the cavity, likely corresponding to vortices advected from the impingement back upstream *via* the main recirculation. Note that similar results were obtained for the case $L/D = 2.0$, $L/\theta_0 = 96$ in Ref. 37.

Once the mean-flow is obtained, cross-stream velocity profiles $\overline{U}_x(y)$, at different abscissas x, are fitted with an hyperbolic-tangent profile of the form:

$$\overline{\mathcal{U}}(y) = U_m + \frac{\Delta U}{2}\tanh\left(\frac{2(y - y_c)}{\delta_\omega}\right), \tag{8}$$

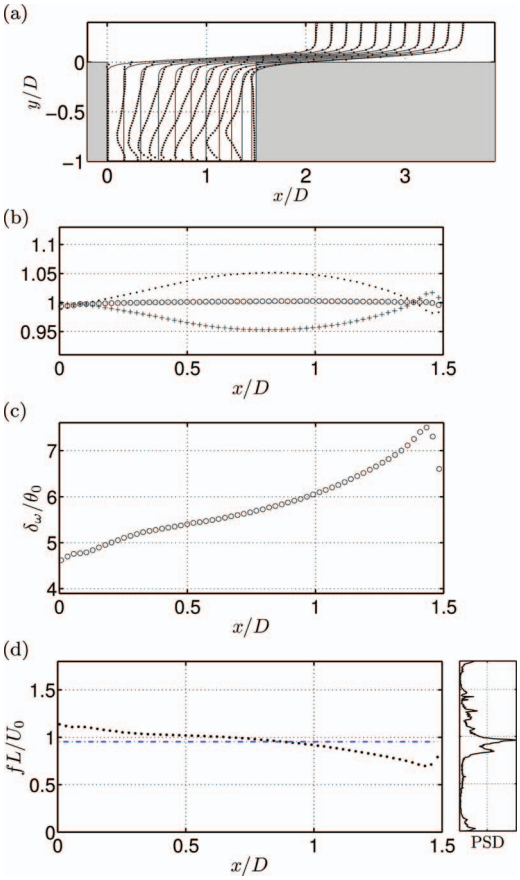

FIG. 5. Shear-layer local features along streamwise coordinate x/D: (a) cross-stream profiles fitted by a hyperbolic-tangent law; (b) twice the mean velocity $2U_m$ (·), shear strength ΔU (+), and $U_1 = \overline{U}_x(y \to +\infty)$ (○); (c) vorticity thickness δ_ω/θ_0; (d) the most destabilizing frequency $f_c = 0.44\, c/(\pi\, \delta_\omega)$ (·), estimated as in a free shear layer, the wave celerity being given by $c = U_m(x)$, and the dominant frequency $f_a L/U_0 = 0.96$ (– · –) of the spectrum (on the right).

where the shear-layer vorticity thickness δ_ω is defined as

$$\delta_\omega = \frac{\Delta U}{\left(\frac{\partial \mathcal{U}}{\partial y}\right)_{\max}}. \tag{9}$$

The fit is performed by minimizing its $\mathcal{L}_2$-norm difference with the mean cross-stream profile, for which the shear layer region only is considered ($-0.4 \le y/D \le 0.4$). Examples of fitted profiles are provided in Fig. 5(a). The inflexion point is determined at $y = y_c$, such that the gradient $(\partial \overline{U}_x/\partial y)$ is maximum, by definition. In addition, $\overline{U}_x(y_c)$ corresponds to the average velocity $U_m = (U_1 + U_2)/2$. The extrema velocities are defined as $U_1 = \overline{\mathcal{U}}(y \to +\infty)$ and $U_2 = \overline{\mathcal{U}}(y \to -\infty)$, respectively. The shear-strength is given as $\Delta U = U_1 - U_2$. U_m and ΔU clearly exhibit a variation along the shear layer due to the evolution of $U_2(x)$ implied by the recirculating flow, see Fig. 5(b). In Fig. 5(c), the vorticity thickness at the leading edge is $\delta_{\omega 0} = 4.6\theta_0$, which reasonably satisfies the theoretical properties of Blasius-profile mixing layers, as defined by Monkevitz and Huerre.[49] Then, δ_ω shows a monotonic increase along the shear layer ($4.6 \le \delta_\omega/\theta_0 \le 7.5$), until very close by the impingement. That evolution matches the results in literature from experiments by Sarohia[6] to the two-dimensional numerical simulations in Rowley *et al.*[39]

Once such characteristics have been obtained, the most amplified frequency associated with each hyperbolic-tangent profile $\overline{\mathcal{U}}(y)$ can be estimated. Following Michalke[50,51] and Huerre and

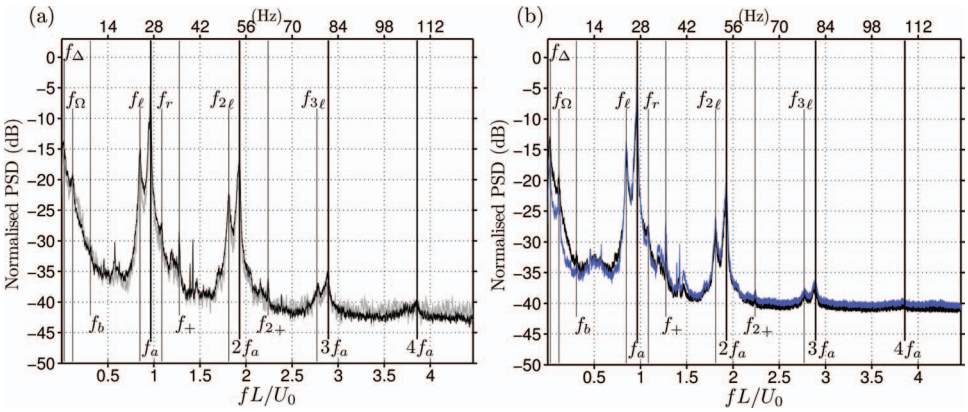

FIG. 6. Normalized power spectral distribution of (a) u' from LDV (black) together with an averaged PSD over the 15 PIV series (gray) extracted at the LDV point ($x/D = 1.4$, $y/D = 0.1$); (b) fluctuations u' (black) and v' (gray, blue), out of the PIV time series and space-averaged over the impingement vicinity ($1.3 \leq x/D \leq 1.5$ and $-0.23 \leq y/D \leq 0.23$). Line thickness corresponds to the 99%-confidence interval.

Rossi,[52] the critical frequency f_c in a free shear layer satisfies the condition:

$$\mathrm{St}_c^{\delta_\omega} = f_c \delta_\omega / U_m = 0.445/\pi. \tag{10}$$

The neutral mode (zero growth-rate) is given by $\mathrm{St}_m^{\delta_\omega} \simeq 0.32$. As well as both $U_m(x)$ and $\delta_\omega(x)$, f_c is expected to be a function of streamwise position x/D. It actually shows a decrease along the shear layer in Fig. 5(d). However, those results must be interpreted with caution, since the characteristics of the shear layer are obtained from a saturated state instead of the actual base-flow. Furthermore, the present stability study theoretically applies to free shear layers considered as two-dimensional parallel flows. Such assumptions are intrinsically ruled out by the impingement at the trailing corner and the inner-cavity flow, responsible for the emergence of global stability properties. Nevertheless, let us remark that the dominant frequency $f_a = 27$ Hz, as seen in Fig. 6, rises within the range described by the estimated critical frequency $f_c(x)$. In fact, averaging f_c over the cavity length gives $\langle f_c \rangle_L = 26.7$ Hz $\simeq f_a$. Such a match is coherent with the parametric evolution obtained in Fig. 3. The empiric Strouhal number St_*^L is fairly close to St_a^L for the case under study.

IV. LOCAL ANALYSIS: SPECTRAL SIGNATURE

A. Power spectra

The present section aims to identify the various frequencies constituting the time-evolution of the flow using spectral analysis of both LDV and time-resolved PIV time-series. Although performed in the very same experimental configuration, LDV and PIV measurements are neither time-synchronized nor simultaneous. Therefore, instantaneous events cannot be compared with the two methods. The reproducibility of the phenomenon at work can however be confirmed by comparing spectral distributions. Four LDV recordings have been acquired each over about 300 s. By averaging over 6500 Hamming-windows of about 18 s, we end up with a frequency step $\delta f_{ldv} = 0.056$ Hz and a 99%-confidence interval [$\simeq \pm 0.14$ dB]. Note that confidence intervals are computed using χ^2-distributions of probability. PIV spectra are built over 15 independent records of 21 s long each. For each record, the time series is extracted from the collection of TR-PIV fields, at the LDV measurement-point. Averaged spectrum is performed over 750 windows of 10.5 s providing a frequency step $\delta f_{piv} = 0.095$ Hz and a 99%-confidence interval [$-0.400.41$ dB]. In Fig. 6(a), LDV and PIV spectral structures are quasi identical. The signal over noise ratio is about 35 dB for the dominant mode in both PIV and LDV measurements. Note also that the mean value $\overline{U}_x$ of $U_x(t)$ are equal within 0.1% for both the LDV and PIV time-series. Strouhal numbers of the present study are circled in gray (red) in the parametric study shown in Fig. 3. The dominant mode is found at frequency $f_a = 27.0$ Hz, corresponding, as expected, to a Strouhal number close to 1

($\mathrm{St}_a^L = f_a\,L/U_0 = 0.96$). Side-band peaks also exist, the most energetic being observed to the left of f_a at $f_\ell = 23.7$ Hz (Strouhal number $\mathrm{St}_\ell^L = f_\ell\,L/U_0 = 0.85$). f_ℓ counterparts to the right of f_a, $f_r = 30.4$ Hz is barely discernible. The difference frequency, $f_a - f_\ell$, is also observed in spectra of Fig. 6 at $f_\Omega = 3.3$ Hz. The versatility of f_Ω can be up to about 0.7 Hz from one experiment to another. Furthermore, this frequency f_Ω does not show up systematically in experiments. It may occur that this component is absent from the flow over long periods of time. The Strouhal number associated with f_Ω is $\mathrm{St}_\Omega^L = f_\Omega L/U_0 = 0.12$ when based on L, $\mathrm{St}_\Omega^D = f_\Omega D/U_0 = 0.078$ when based on D. At this stage, one cannot determine whichever of L or D is the relevant length scale, since the physical meaning of f_Ω is not known yet. In any case, frequency ratios $f_\Omega/f_a = 0.12$ and $f_\ell/f_a = 0.88$ are unusual ratios for rectangular open cavity flows, see Refs. 12 and 15. It rather looks like an intermediate regime, as it is only observed over a very small range of parameters. Power spectral densities based on velocity fluctuations are quite similar – see Fig. 6(b) – regardless of the velocity component, u' (dark) or v' (gray, blue). The most striking difference comes from low-frequency range, where energy levels are higher for u' than for v'. Spectra based on v' exhibit some additional features, hardly seen in spectra based on u'. For instance, the right side-band peak $f_r = 30.4$ Hz $\simeq f_a + f_\Omega$ ($\mathrm{St}_r^L = f_r\,L/U_0 = 1.08$) is more easily distinguished. The existence of such two side-band peaks with different amplitudes, f_ℓ and f_r, is a typical feature of open cavity flows. It indicates an asymmetrical amplitude modulation of f_a by f_Ω.

For a lower part, another side-band peak can be mentioned to the right of f_a, at $f_+ = 35.7$ Hz, corresponding to $\mathrm{St}_+^L = 1.28$, is roughly aligned with the line $\mathrm{St}^L \simeq 3/2$ ($n = 3$) in Fig. 3. That frequency, along with $f_{2+} = 62.7$ Hz ($\mathrm{St}_{2+}^L = 2.25$), could be associated with a modulating (edge) frequency $f_b = f_+ - f_a = f_{2+} - 2f_a = 8.6$ Hz, yet not seen in spectra. Indeed, the ratio $f_b/f_a \simeq 0.32$ and Strouhal number $\mathrm{St}_b^L = 0.31$ suggest a connection with shear layer impingement, see Refs. 12, 14, 15, and 37. In addition, the dominant mode at f_a generates harmonics at $2f_a$ and $3f_a$, on the contrary to f_ℓ, for which no harmonic is observed. On the other hand, side-band peaks are observed to the left of the harmonics, at $f_{2\ell} = 2f_a - f_\Omega$ and $f_{3\ell} = 3f_a - f_\Omega$. The same applies to frequencies $f_+ = f_a + f_b$ and $f_{2+} = 2f_a + f_b$. The overall scheme, therefore, confirms the existence of two different amplitude modulations, by f_Ω and f_b, respectively, and only one carrier frequency at f_a. The strength of the side-band peak, at f_ℓ, compared to the one at f_+ indicates that the modulation process, at f_Ω, overwhelms the interaction between f_a and f_b.

Finally, a broad-band peak rises at very low frequencies, between 0.2 Hz and 0.9 Hz, in the LDV spectrum of Fig. 6(a). It restricts to a narrower peak at the frequency $f_\Delta = 0.67$ Hz ($\mathrm{St}_\Delta^L = 0.024$, $\mathrm{St}_\Delta^D = 0.016$) in the v'-spectrum of Fig. 6(b). The rather small scale of those Strouhal numbers will be dealt with in Sec. VI C.

B. Time-frequency analysis

Spectra only give a statistical information on flow spectral features. To go one step further, a time-frequency analysis is required. Figure 7 shows time-series and time-frequency diagrams for velocity fluctuations u' and v' extracted from point ($x/D = 1.44$, $y/D = 0$) out of the time-resolved velocity fields. This point is located in the very peculiar top-plane of the cavity, in the core of the shear layer, just upstream of the impinging corner. Both $u'(t)$ (light) and $v'(t)$ (dark) time-series are displayed in Fig. 7(a). Their corresponding time-frequency diagrams are shown in Figs. 7(b)–7(c).

Both time-frequency diagrams, when considered altogether, show that the peak at f_a, although varying in amplitude, is present at almost any time. By contrast, f_ℓ is partially present in time-frequency diagrams and does not enter in competition with f_a. Frequencies f_a and f_ℓ therefore do not experience mode-switching to the difference of what was observed in Lusseyran *et al.*[17] and Pastur *et al.*[16] On the other hand, the right side-band frequency $f_+ = 35.7$ Hz $\simeq f_a + f_b$ ($\mathrm{St}_{a+b}^L = 1.28$), of small amplitude when averaged over the observation time, sporadically appears and competes with f_a (for instance, at times $t = 5$, 8.5, 11, 12.5 s). As a result, self-sustained oscillations are largely reduced in amplitude during such periods.

Time series of Fig. 7(a) exhibit several time-scales. In $v'(t)$ (dark curve), the carrier, at f_a, is strongly modulated in amplitude by broad-banded low frequency components. The main modulating

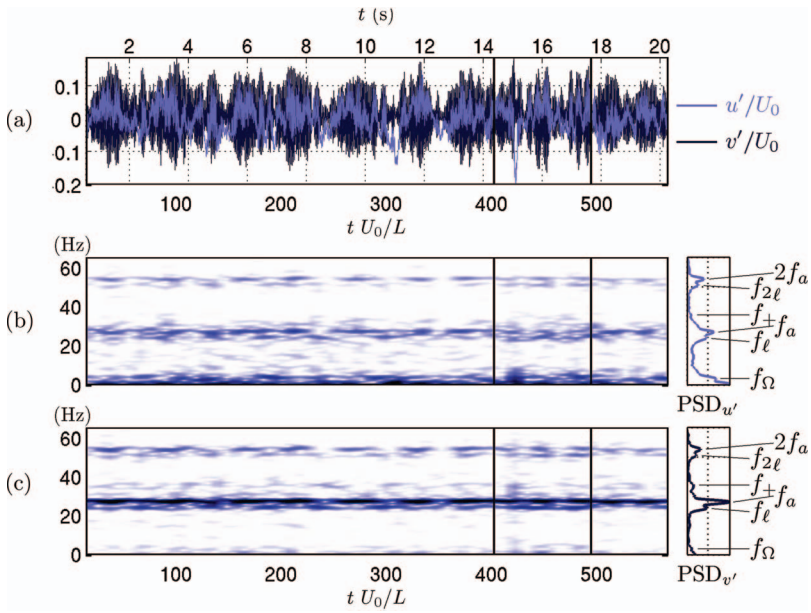

FIG. 7. (a) TR-PIV time-series for configuration $L/\theta_0 = 76$ for both fluctuating velocity components u'/U_0 (light) and v'/U_0 (dark) extracted at point ($x_p/L = 0.96$, $y_p/D = 0$); and their corresponding time-frequency diagrams for (b) u'/U_0 and (c) v'/U_0, respectively. Vertical black lines delimit the time-window used for Sec. V B.

frequency is $f_\Omega = 3.3$ Hz. Time-frequency diagram for v', in Fig. 7(c), exhibits no low frequency components to the benefit of side-band-peaks, f_ℓ and $f_{2\ell}$, such that $f_\Omega \simeq f_a - f_\ell = 2f_a - f_{2\ell}$. On the contrary, low frequencies rather sum up to f_a oscillations for $u'(t)$ (light curve in Fig. 7(a)). Indeed, the corresponding time-frequency diagram of Fig. 7(b) shows much energy for low frequency-components, f_Ω and the broad-band peak around f_Δ. In other words, the amplitude modulation process can be considered as not complete for u'.

V. SPACE-TIME EVOLUTION

A. Shear-layer wave properties

Various frequency peaks have been identified as related to shear layer modes. Such progressive waves have yet to be characterized. Indeed, since the velocity fields are both spatially and temporally resolved, it is possible to directly estimate the wavelength and phase-velocity associated with a given frequency within the shear-layer. Considering two points at x_1 and x_2 in the shear-layer, shifted by $\Delta x = x_2 - x_1$, the transfer-function $T_{12}(\omega)$ between the two points can be determined for any frequency $f = \omega/(2\pi)$. A good estimate for the transfer function, between an input signal $v_1(t)$ (velocity at point x_1) and an output signal $v_2(t)$ (velocity at point x_2), can be defined as

$$T_{12}(\omega) = \frac{P_{21}(\omega)}{P_{11}(\omega)}, \tag{11}$$

where $P_{21}(\omega)$ is the cross spectral distribution between signals u_2 and u_1:

$$P_{21}(\omega) = \sum_{m=-\infty}^{+\infty} R_{21}(m)e^{-i\omega m}, \tag{12}$$

which involves the cross-correlation function R_{21},

$$R_{21}(\Delta t) = E[u_2(t+\Delta t)u_1^*(t)] = E[u_2(t)u_1^*(t-\Delta t)], \tag{13}$$

based on the estimated value $E[\cdot]$ of the quantity under brackets. Estimator $E[\cdot]$ can simply be reduced to the time average operator as in Rockwell.[53] The transfer function

$$T_{12}(\omega) = G(\omega) \cdot e^{i\phi(\omega)},$$

with gain G and phase shift ϕ, must be used with some care. Indeed, at frequencies $f = \omega/(2\pi)$ where the spectral density is vanishing, that is, when $P_{11}(\omega) \to 0$ in Eq. (11), the quantity $T_{12}(\omega)$ is not well-defined and only frequencies that significantly contribute to the spectrum should be considered. In the following, we will consider the cavity dominant frequency and its first harmonic along with the most energetic side-band peaks. Transfer functions are estimated on crosswise component v' in the shear layer because it exhibits larger oscillations than those of the streamwise component u', as seen in Fig. 7. Estimate is performed for different streamwise x-positions, at depth $y/D = +0.05$, where turbulence intensity is maximum. Phases along x are referenced with respect to the signal at $x_0/L = 0.5$ (where $\phi = 0$) because the velocity fluctuations are too weak to provide a clean reference point at the cavity leading corner, $x/L = 0$. Similarly, at $x/L = 1$, boundary effects at the trailing corner may alter the phase. At mid-length, spectrum exhibits strong peaks, and the fluctuations are still exponentially increasing with space indicating that linear instability approximation stands and non-linear effects do not play a significant role yet. Transfer functions are estimated at points distant by a multiple of $\delta x/L = 0.016$ from the reference point ($x_0/L = 0.5$). The plus/minus sign depends on whether the point under consideration is downstream or upstream relatively to the reference point.

In Fig. 8(a), the unwrapped phase $\phi(x)$ is shown with respect to x/L for the main frequencies of the shear layer oscillations. First consider the dominant frequency $f_a = 27.0$ Hz($\mathrm{St}_a^L = 0.96$). The phase $\phi_a(x)$, associated with $\omega_a = 2\pi f_a$, varies quasi-linearly along the shear layer. Overall phase

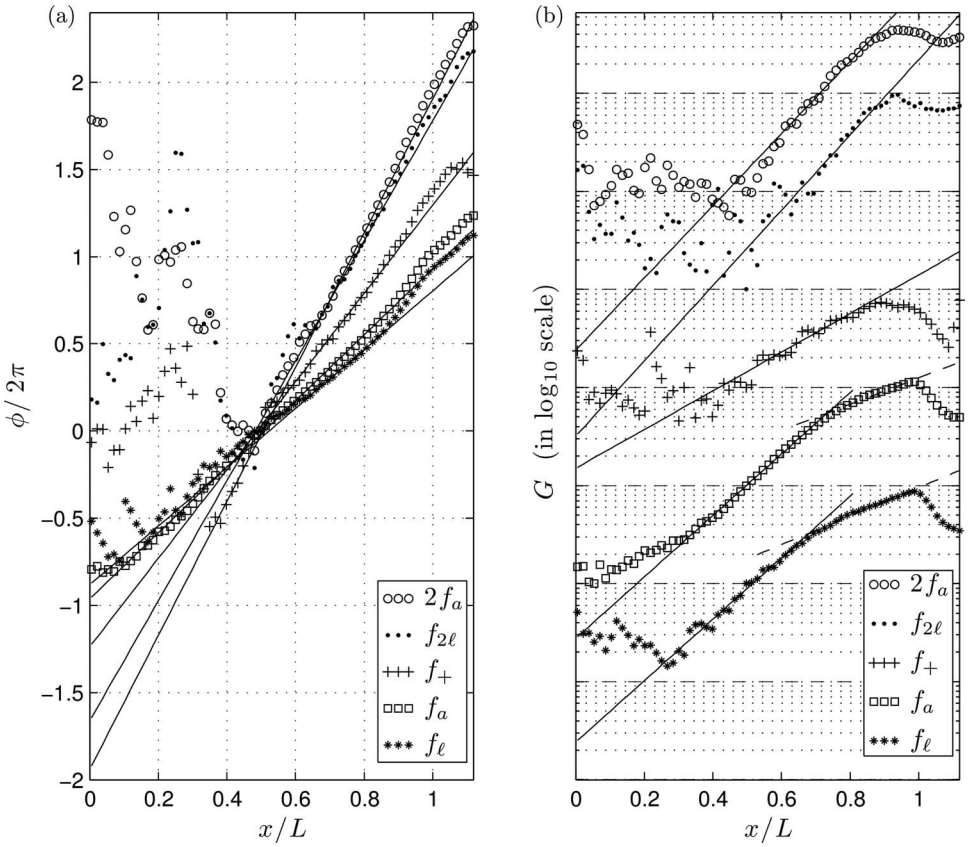

FIG. 8. Wave properties of the main frequencies of the flow along the shear layer. (a) Phase evolution with respect to x/L, solid lines corresponding to linear fits. (b) Amplitude variation with respect to x/L. Contributions are shifted vertically for the sake of legibility and straight lines correspond to fits of the exponential form $e^{\beta(x-x_0)}$. See text for details.

variation from separation to impingement is close to 4π indicating that the wavelength is of the order of $L/2$. More precisely, one may compute a linear regression of the form,

$$\phi_a(x) = \alpha(\omega_a)x + \gamma(\omega_a), \tag{14}$$

from $x/L = 0.15$ to $x/L = 0.86$ such as to avoid boundary effects. It gives an estimated mean dimensionless phase gradient $k_a\, L = L(\partial\phi_a/\partial x)_{\text{mean}} = 3.8\pi$ for f_a. Space-shift Δx matches with wavelength when the phase difference $\Delta\phi = 2\pi$, which occurs for

$$\lambda_a = \frac{2\pi}{\left(\frac{\partial\phi_a}{\partial x}\right)_{\text{mean}}} \tag{15}$$

giving $\lambda_a/L = 0.53 \simeq 1/2$. Moreover, the phase velocity defined for f_a as

$$c_a = \frac{\omega_a}{\left(\frac{\partial\phi_a}{\partial x}\right)_{\text{mean}}} \tag{16}$$

can be estimated at $c_a = 1.07$ m/s $\simeq U_0/2$. For the harmonic $2f_a$, the phase is not defined before $x/L \simeq 0.5$ (see Fig. 8(a)). That is, coherent with the spatial structures shown later in Sec. VI. Fitting the phase $\phi(\omega_{a2}, x)$, associated with $2f_a$ $\phi(\omega_{a2}, x)$, over the range $0.5 \leq x/L \leq 0.86$ gives the phase gradient (wavenumber) $k_{a2}\, L = L(\partial\phi/\partial x)_{\text{mean}} = 7.7\pi$. The resulting wavelength is therefore $\lambda_{a2}/L = 0.26$, which implies a phase velocity $c_{a2} = 1.06$ m/s. Considering λ_{a2} as the first harmonic of mode λ_a, i.e., $\lambda_{a2} = \lambda_a/2$, one gets an average mode wavelength $\lambda/L \simeq 0.52$. This defines an actual cavity length $L_{\text{eff}} = 2\lambda$ such that $L_{\text{eff}} = (1+\epsilon)L$, with $\epsilon = 4\%$. This *effective length* may be understood as the length the cavity should have to enhance the selected dominant mode if the impinging corner were inducing no contraction of the wave front. As expected, phase velocities c_a and c_{a2}, for the dominant mode f_a and its harmonic $2f_a$, are equal (non-dispersive medium with respect to the dominant wave). The same analysis can be done for the two left side-band peaks, $\text{St}_\ell^L = 0.85$ ($f_\ell = 23.7$ Hz) and $\text{St}_{2\ell}^L = 1.81$ ($f_{2\ell} = 50.8$ Hz). Data points are fit from $x/L = 0.66$ to $x/L = 0.86$. It comes $c_\ell = 1.06$ m/s, $\lambda_\ell/L = 0.59$, and $c_{2\ell} = 1.11$ m/s, $\lambda_{2\ell}/L = 0.29$. Finally, the right side-band frequency $f_+ = 35.8$ Hz exhibits the phase velocity $c_+ = 1.05$ m/s and wavelength $\lambda_+/L = 0.40$. All estimated phase velocities for both carrier and side-band frequencies are therefore equal to $U_0/2$, within 2% dispersion. This was expected for shear layer modes, which arise from a Kelvin-Helmholtz-like instability.

The spatial growth rate $\beta(\omega)$ of unstable propagating waves (ω, k) can be estimated from transfer functions as

$$\beta(x) = \left(\frac{\partial\ \ln|G(\omega, x)|}{\partial x}\right)_\omega. \tag{17}$$

Before saturation and distortion nearby the trailing edge of the cavity, the shear layer modes are linearly unstable (see Basley[38] for more examples). As a result, β is basically constant along x, such that the amplitude of the mode grows exponentially as $e^{\beta(x-x_0)}$. In Fig. 8(b), linear regressions on $(\partial\ln|G(\omega, x)|/\partial x)$ are performed from $x/L = 0.32$ to $x/L = 0.71$ for f_a and from $x/L = 0.60$ to $x/L = 0.89$ for $2f_a$. It comes $\beta_a\, L = 7.2$ and $\beta_{a2}\, L = 8.5$. Concerning the two left side-band peaks f_ℓ and $f_{2\ell}$, growth rates are $\beta_\ell\, L = 7.2$ (fit for $0.41 \leq x/L \leq 0.63$) and $\beta_{2\ell}\, L = 8.8$ (fit for $0.60 \leq x/L \leq 0.89$), respectively, (Fig. 8(b)). However, it is possible to identify another smaller growth rate for both f_a and f_ℓ when considering the amplitude evolution further downstream, that is, for $0.7 \leq x/L$. Exponential fits are represented by dashed lines in Fig. 8(b) and correspond to growth rates $\beta'_a L = 3.1$ and $\beta'_\ell L = 3.3$. In fact, the slopes change at about $x/L = 0.7$ exactly where the modes associated with $2f_a$ and $f_{2\ell}$ start being spatially coherent and increasing in energy. Therefore, it is suspected that lower spatial growth rates beyond $x/L > 0.7$ may result from an energy transfer from the modes at f_a and f_ℓ towards the modes $2f_a$ and $f_{2\ell}$, *via* non-linear interactions (f_a, f_a) and (f_ℓ, f_a), respectively. Finally, all growth rates decrease again close to the downstream corner $(x/L \to 1)$ likely due to the deflection of the wave at the impingement. Table II summarizes all shear layer waves characteristics discussed in this section.

TABLE II. Wave properties measured at $y/D = 0.05$.

Mode	fL/U_0	c/U_0	λ/L	kL	βL
ℓ	0.85	0.51	0.59	3.4π	$7.2 - 3.3$
a	0.96	0.51	0.53	3.8π	$7.2 - 3.1$
$+$	1.28	0.50	0.40	5.1π	4.5
2ℓ	1.81	0.53	0.29	6.9π	8.8
$a2$	1.92	0.50	0.26	7.7π	8.5

B. Space-time structures and inner-flow interactions

In order to describe the shear layer flapping motion as well as its interactions with the inner-flow, various space-time representations are employed. The sample under study is a close-up extracted from the very same 21 s long time-series priorly used in Sec. IV B. The new time-range is enclosed between two vertical black lines in Fig. 7 and lasts over 3.5 s, i.e., $400 < t\frac{U_0}{L} < 495$ in dimensionless time units.

As a visual and qualitative approach, a (x, y, t)-volume is depicted in Figs. 9 and 10 in which iso-surfaces of spanwise vorticity fluctuations $\omega_z' L/U_0$ are displayed. Negative and positive vorticity structures are dark and light, respectively (blue and yellow). Such a 3D representation uses t-axis as a third (*spanwise*) dimension. Two-dimensional eddies, existing in an xy-plane, therefore appear as 3D-tubes.

Self-sustained oscillations of the shear layer are observed around the impingement, at frequency f_a, and are amplitude modulated by a low frequency—see Fig. 9. Shear layer vortices traveling and impinging onto the downstream corner of the cavity imply periodic inflows injected along the downstream wall. In fact, the resulting stream downwards the cavity fluctuates depending on amplitude modulations of the flapping shear layer: larger oscillations at the impingement correspond to stronger inflows hence increase the stream. Whereas shear layer (carrier) frequency oscillations shortly disappear further from the downstream wall, a few stronger structures are indeed encountered at a larger time scale, in Figs. 9 and 10. These large scale structures (corresponding to low frequencies) are advected upstream around the main recirculation. In particular, the sinus-shape they describe when seen from below confirms a circular trajectory – see Fig. 10(b). Positive vorticity *tubes* seem to develop closer to the walls, likely enhanced by positive velocity-gradients inside the boundary layers. For similar reasons, negative vorticity structures remain at a smaller radius inside the main vortex.

For more quantitative aspects, Fig. 11 consists of extracted *space-time planes* and times-series at key locations inside the cavity, as shown in Fig. 11(f). Streamwise space-time diagrams are built at three different positions y/D in Figs. 11(a), 11(b), and 11(c). They display contours of vorticity fluctuations. Vertical and horizontal axes represent dimensionless time $t\frac{U_0}{L}$ and streamwise coordinate x/L, respectively. Similarly, Figs. 11(d) and 11(e) represent two crosswise space-time diagrams, whose horizontal and vertical axes are dimensionless time $t\frac{U_0}{L}$ and crosswise coordinate y/D, respectively. Phase-velocities of the shear-layer waves can be estimated from slopes depicted by space-time structures. Streamwise component $c_x = \Delta x/\Delta t$ from Figs. 11(a)–11(c), and crosswise component $c_y = \Delta y/\Delta t$ from Figs. 11(d) and 11(e). Local insight of the temporal behavior is provided by time-series extracted from three intersections of the space-time planes, (a)–(e). The first time-series is picked up at the intersection of planes (a) and (d) in the shear layer—see Fig. 11(a ∩ d). The time-series in Fig. 11(b ∩ d), at the intersection of planes (b) and (d), characterizes the inflow along the downstream wall of the cavity. Finally, Fig. 11(c ∩ e) yields the temporal dynamics extracted from the main recirculation. Both components of velocity fluctuations are plotted and normalized by U_0.

Shear layer oscillations appear in Figs. 11(a) and 11(a ∩ d). The modulating frequency can easily be identified as f_Ω. As expected, vortices of alternative sign traveling downstream along cavity top plane constitute a *fast wave* whose associated phase velocity, c_a, is fairly constant along the shear layer. In Fig. 11(a), the slope gives $c_a \simeq 0.5U_0$, as already pointed out in Sec. V A. Like

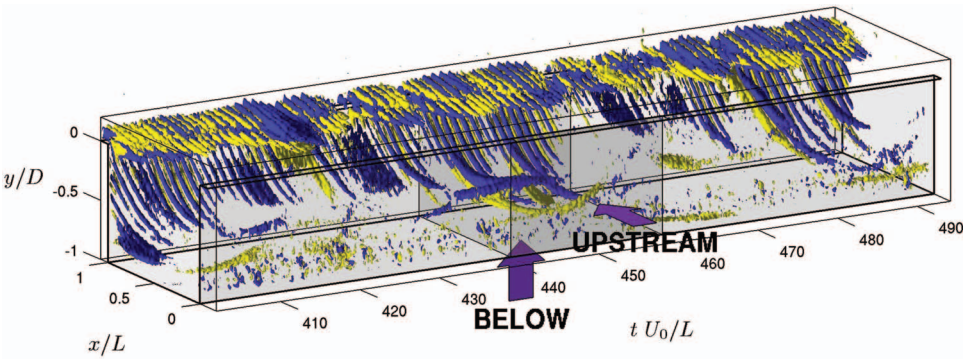

FIG. 9. Iso-surfaces of vorticity fluctuations in the space-time volume (x, y, t), issued of time-resolved PIV data for configuration $L/\theta_0 = 76$. $\omega_z' L/U_0 = 1.6$ (light, yellow) and $\omega_z' L/U_0 = -1.6$ (dark, blue). Only an abstract of the entire set, such as $400 < t\frac{U_0}{L} < 495$, is displayed.

the streamwise-traveling vortices of the shear layer, the signature of crosswise-traveling eddies, modulated in amplitude, is observed along the downstream wall—see Fig. 11(d). In the time-series plotted in Fig. 11(b ∩ d), the axis-wise projection (v') exhibits the modulating frequency f_Ω, while transverse fluctuations (u') contain most of their energy at the carrier frequency f_a and are modulated in amplitude. These eddies are advected at a lower velocity than along the shear layer. The large scale fluctuations identified in the (x, y, t)-volume (Figs. 9 and 10) can here be recognized as

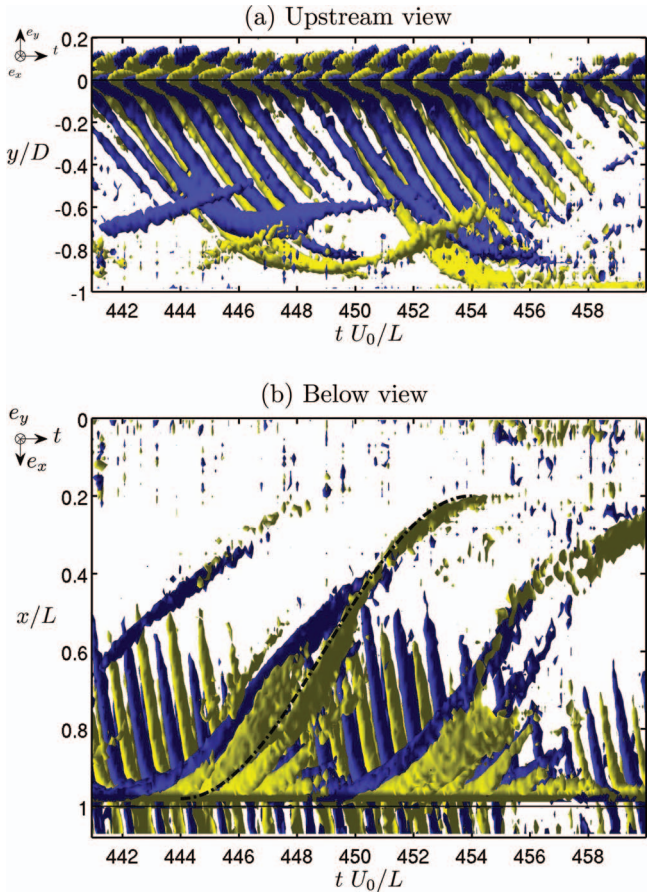

FIG. 10. A close-up ($441 < t\frac{U_0}{L} < 460$) from Fig. 9, shown from upstream (a) and below (b).

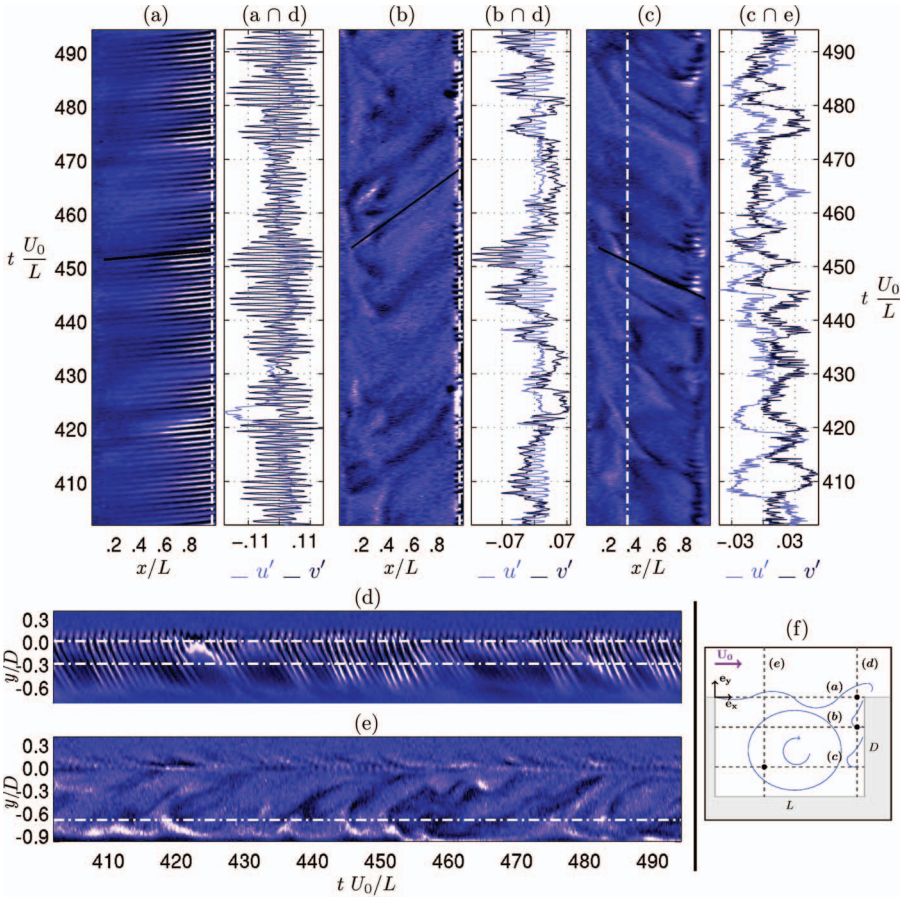

FIG. 11. Space-time diagrams and time-series issued of time-resolved PIV data for configuration $L/\theta_0 = 76$, with the same close-up in time as Fig. 9 ($400 < t\frac{U_0}{L} < 495$). The space-time diagrams are obtained at (a) $y/D = 0$, (b) $y/D = -0.3$, (c) $y/D = -0.7$ (streamwise) and at (d) $x/L = 0.96$, (e) $x/L = 0.33$ (crosswise). Contour levels of vorticity fluctuations $\omega_z' L/U_0$ range from (a) −4 (dark)–5.5 (light); (b) −2–2.2; (c) −3–4; (d) −5–5; and (e) −2–2. Three characteristic time-series, for both streamwise and crosswise velocity fluctuations u'/U_0 and v'/U_0, are extracted at intersections of these space-time planes: at the impingement, (a ∩ d); in the inflow along the downstream wall, (b ∩ d); inside the main recirculation, (c ∩ e). Schematic (f) locates extraction regions.

traveling upstream in Fig. 11(c) and upwards in Fig. 11(e), and corresponding to low frequency oscillations in time-series (c ∩ e). In addition, the phase velocity extracted from space-time domain of Fig. 11(b), that is just below the shear layer, is found around $c_{cav} \simeq 0.12$ m/s which gives the ratio $\eta = c_{cav}/c_a \simeq 0.11$. Such a relation may not be fortuitous, since it is, within uncertainties, equal to f_Ω/f_a. This suggests that the main oscillator (the shear-layer) and the secondary one (the inner-flow recirculation) could be phase-locked in a ratio close to $\eta = 0.11$. As a result, the amplitude modulation of shear layer flapping motion is related to a low frequency wave (at f_Ω) propagating inside the cavity along the main recirculation.

VI. MODAL DECOMPOSITION

The identification of the coherent structures constitutive of the flow continues with Fourier mode decomposition, which enables us to segregate space from time scales. When applied to spatially extended data, such as time-resolved velocity fields, the *global Fourier* decomposition provides a set of spatial structures (or modes), each of them associated with one frequency (see for instance Basley *et al.*[37] and Rowley *et al.*[39]).

Successive snapshots issued of a time-resolved PIV experiment are ranked in a space-time dataset as follows:

$$\mathcal{V}_1^N = \{\mathbf{u}'(x, y, t_1), \mathbf{u}'(x, y, t_2), \ldots, \mathbf{u}'(x, y, t_N)\}, \tag{18}$$

with $N = 5242$ and $t_N \simeq 21$ s. Global Fourier modes are obtained by Fourier-transforming time-series $g(t)$, produced at each spatial point (x, y) of the fluctuating velocity field, $g(t) = u'(x, y, t)$ or $g(t) = v'(x, y, t)$ depending on the component under consideration. By combining each local Fourier transform, into a 2D-2C field defined on the spatial grid (x, y), one ends up with spatial structures, $\mathbf{F}(\mathbf{r}, f)$, ranked in the new space-frequency dataset:

$$\begin{aligned}\mathcal{F}_1^N = \{&\mathbf{F}(x, y, -f_{N/2}), \mathbf{F}(x, y, -f_{N/2-1}), \ldots,\\ &\mathbf{F}(x, y, f_{N/2-1}), \mathbf{F}(x, y, f_{N/2})\},\end{aligned} \tag{19}$$

where $f_k = k/(N\Delta t)$ is the frequency-channel, such that $0 \leq k \leq N/2$. The frequency step is therefore inferior to 0.05 Hz. More details about the methodology can be found in Refs. 37 and 38. In the following, note that Fourier modes write simply as $\mathbf{F}_k(x, y) = \mathbf{F}(x, y, f_k)$.

Remark that dynamic mode decomposition of $\mathcal{V}_1^N$ could be performed on the very same dataset. Dynamic mode decomposition methods are discussed in detail in Schmid,[54] Rowley *et al.*,[55] and Duke *et al.*[56,57] Contrary to Fourier modes, dynamic modes would be associated with growth or decay rates. In other words, eigenvalues of the operator of evolution can depart from the unit circle. This is particularly insightful when describing transient dynamics. However, the present investigation deals with a fully saturated (permanent) regime. As a result, the system exhibits pseudo-periodic dynamics evolving around a limit cycle. In such a state, global Fourier modes and dynamic modes are quasi-identical, as demonstrated in Ref. 55, though the frequency step may not be constant for dynamic modes.

A. Shear layer modes

The coherent structures associated with the dominant frequency f_a and its harmonic $2f_a$ are shown in Figs. 12(a)–12(d). The real part of global Fourier modes is shown in the left column, the imaginary part in the right column. The spatial structures associated with the left side-band peaks f_ℓ and $f_{2\ell}$ are shown in Figs. 12(e)–12(h) and those which correspond to the right side-band peak at f_+ ($\mathrm{St}_+^L = 1.28$) are displayed in Figs. 12(i) and 12(j). As expected, all are shear-layer modes with energy mainly distributed at the impingement. One observes the wave-like signature of self-sustained oscillations: an alley of counter-rotating vortices saturating when they approach the trailing edge of the cavity, as previously seen in Refs. 37–39. Note the $\pi/2$ shift between imaginary and real parts of the shear layer modes: it indicates a progressive wave. Finally, the wavelengths discerned in shear layer modes are consistent with the results in Sec. V A.

B. Edge interaction $f_b = f_+ - f_a$ ($\mathrm{St}_b^L = 0.31$)

Although $\mathrm{St}_b^L = \mathrm{St}_+^L - \mathrm{St}_a^L = 0.31$ does not appear in spectra, the right side-band peaks at f_+ and f_{2+} would logically suggest such a modulating frequency, as often reported in the literature (Refs. 6, 7, 10–12, 14–16, and 37). Low frequencies f_b are usually measured such that $0.25 \leq f_b L/U_0 \leq 0.4$ and correspond to the gap between regimes of locked-on modes. These *edge* frequencies are imputed to two-dimensional dynamics caused by the vortex-edge interaction, or in other words the phase inconsistency at the impingement. For example, Knisely and Rockwell[12] characterize the frequency $0.4f_a$ as the signature of an amplitude modulation, in connection with cycles of injection/ejection of impacting shear-layer vortices in and out of the cavity, due to the presence of the impingement.

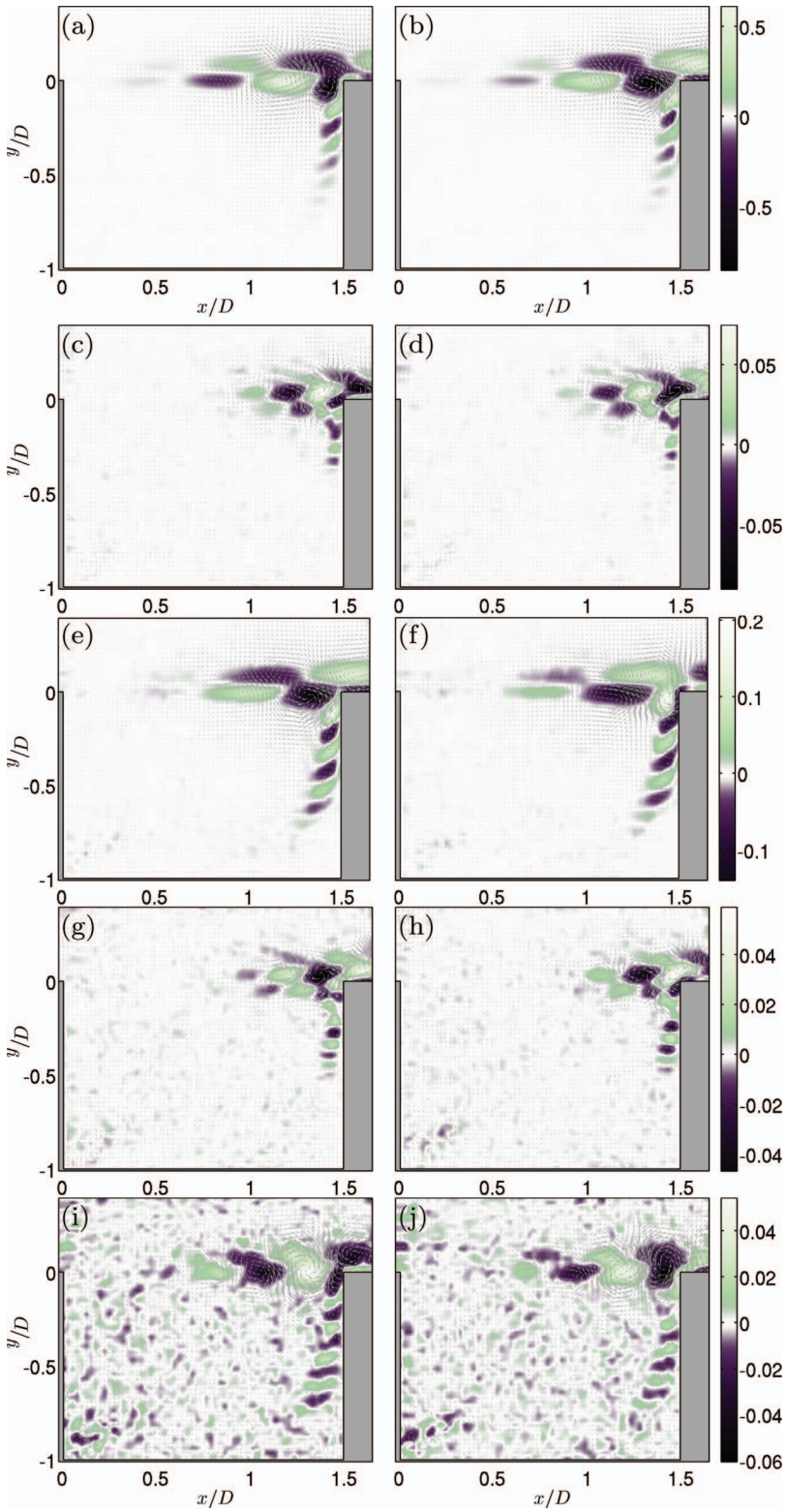

FIG. 12. Real (left) and imaginary (right) parts of global Fourier modes for shear layer frequencies. Arrows represent velocity fluctuations and colors encode vorticity fluctuations normalized by their maximum. (a) and (b) $\mathbf{F}_a(x, y)$ associated with the dominant peak f_a; (c) and (d) $\mathbf{F}_{a2}(x, y)$ associated with its first harmonic $2f_a$; (e) and (f) $\mathbf{F}_\ell(x, y)$ associated with the left side-band peak $f_\ell = f_a - f_\Omega$; (g) and (h) $\mathbf{F}_{2\ell}(x, y)$ associated with the second left side-band peak $f_{2\ell} = 2\,f_a - f_\Omega$; (i) and (j) $\mathbf{F}_+(x, y)$ associated with the right side-band peak $f_+ = f_a + f_b$.

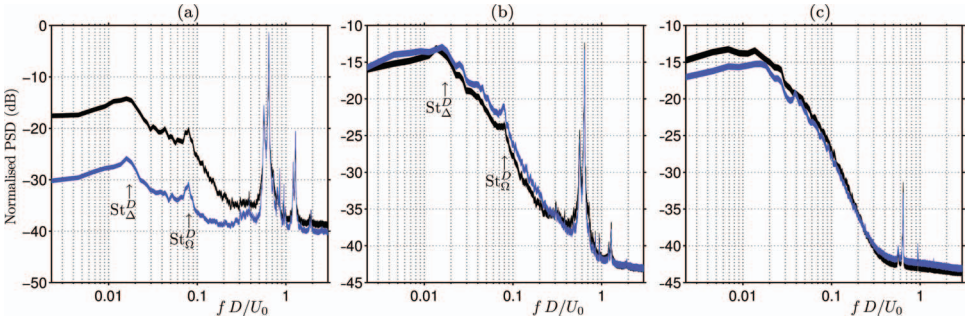

FIG. 13. Space-averaged spectra of velocity fluctuations, u' (black) and v' (gray, blue), out of time-resolved PIV data. Space averaging is performed over three regions of interest of the cross-stream (xy)-plane: above the cavity near the impingement (a), the downstream half of the cavity (b), and the upstream half of the cavity (c). PSDs are displayed as functions of Strouhal number $\mathrm{St}^D = fD/U_0$. Line thickness corresponds to the 99%-confidence interval.

C. Low frequency range and spanwise dynamics

The energy exhibited by open cavity flows in the low frequency range is usually attributed to three-dimensional dynamics prevailing in the inner-flow. As mentioned in Sec. I, the large time-scales of the inner-flow highlighted in the literature of Refs. 28–35, and 38 have been related to centrifugal instabilities and scale on cavity depth D rather than cavity length L. That is the reason why spectra are presented hereafter as functions of the Strouhal number $\mathrm{St}^D = fD/U_0$.

We wish to investigate the spatial organization associated with low frequency dynamics to determine if they are all actually related to spanwise structures or might be due to another feature of the (two-dimensional) primary flow. To focus on low frequencies, Fig. 13 presents spectra for both velocity components u' and v' using a close-up in logarithmic scale. Power spectral densities are obtained from time-resolved PIV data in the cross-stream (xy)-plane and normalized by the maximum energy observed at the LDV point. The window averaging process has been detailed earlier in Sec. IV A.

One must be cautious when dealing with frequencies as low as only one order of magnitude greater than the frequency step because uncertainties increase drastically. Uncertainties are here estimated from the peak half-width: the frequency interval is such that power spectral density is superior to local maximum -3 dB. In order to confirm unambiguously the relevance of such low frequencies, spectra shown in Fig. 13 are space-averaged over large regions of the flow. Three different regions are considered to depict the evolution of the spectral signature from the impingement to the upstream bottom corner of the cavity – displayed in Figs. 13(a), 13(b), and 13(c), respectively.

At the impingement – see Fig. 13(a) – two peaks rise from the broad-band packet.

(i) The frequency f_Ω ($\mathrm{St}^D_\Omega = 0.078 \pm 0.010$): as shown in Secs. II–V, it modulates in amplitude the self-sustained oscillations of the shear layer and is associated with slow inflows traveling from the impingement back upstream inside the cavity.

(ii) The tip of the broad-band peak around f_Δ ($\mathrm{St}^D_\Delta = 0.018 \pm 0.006$): already observed earlier in spectra presented in Figs. 6 and 7, it is also responsible for drastic amplitude modulations of the vortex shedding in the shear layer.

When considering the inner-flow further from the shear layer impingement, shear layer frequencies decrease greatly. Energy level at $\mathrm{St}^D_a = f_a\,D/U_0 = 0.64$ is 50 times smaller in the downstream part of the cavity – Fig. 13(b) – and divided by 1000 in the upstream part – Fig. 13(c). On the contrary, the low frequency range remains strong across the inner-flow, overwhelming the frequency $\mathrm{St}^D_\Omega = 0.078$ in the upstream part of the cavity. A continuum of low frequencies is coherent with a three-dimensional organization of the flow deriving from centrifugal instabilities along the main recirculation.

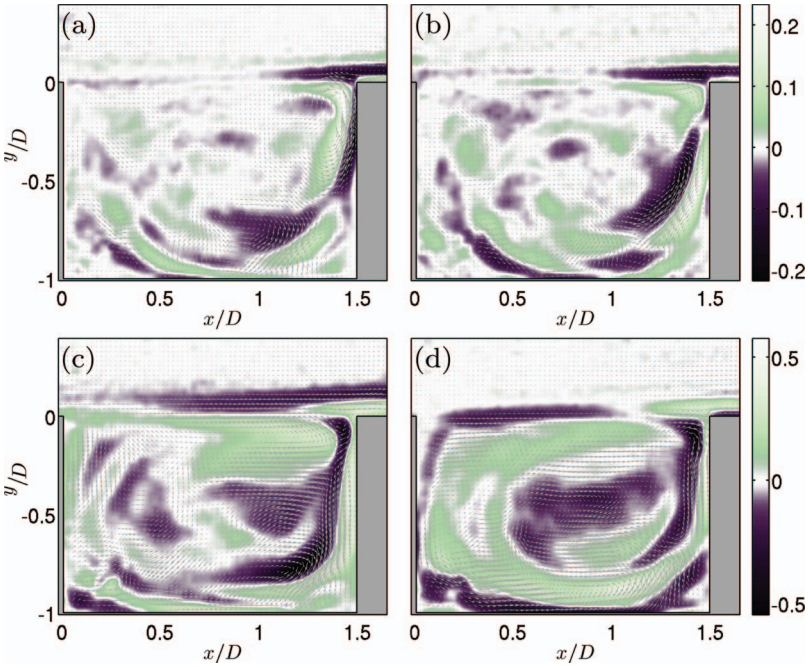

FIG. 14. Real part (left) and imaginary part (right) of global Fourier modes for low frequencies in a cross-stream plane (xy). Arrows represent velocity fluctuations, colors encode vorticity fluctuations normalized by their maximum. (a) and (b) $\mathbf{F}_\Omega(x, y)$ associated with f_Ω; and (c) and (d) $\mathbf{F}_\Delta(x, y)$ associated with f_Δ.

1. Modulating frequency f_Ω ($St^L_\Omega \simeq 0.12$ or $St^D_\Omega \simeq 0.08$)

The regime under investigation presents an amplitude modulation largely overwhelming f_b as shown by the most energetic side-band peaks at $f_\ell = f_a - f_\Omega$ and $f_{2\ell} = 2f_a - f_\Omega$. St^L_Ω is much smaller than modulating Strouhal numbers generally encountered, suggesting another process, possibly three-dimensional. f_Ω is nonetheless still too large to be unambiguously attributed to spanwise-traveling modes inside the cavity. Indeed, corresponding Strouhal number based on cavity depth, $\mathrm{St}^D_\Omega = 0.078$, is much higher than values expected for spanwise centrifugal instabilities – $\mathrm{St}^D_{ci} \leq 0.03$, as detailed in Subsection VI C 2. Consequently, a closer investigation of coherent structures, associated with f_Ω, can provide more insight concerning the phenomenon at play (as in Basley[38]). The global Fourier mode associated with f_Ω, in the cross-stream (xy) plane, is given in Figs. 14(a) and 14(b). It exhibits most of its energy near the impingement and dives into the cavity, where it outlines the main recirculation. Such a spatial organization is similar to those associated with edge frequencies f_b usually encountered.

Since the spatial structure identified in the cross-stream plane does not provide enough information about a possible three-dimensional organization of the mode at f_Ω, additional PIV measurements were conducted in a spanwise plane inside the cavity, as detailed in Sec. II D. From global Fourier decomposition performed on the PIV datasets, no coherent structure associated with the low frequency f_Ω ($\mathrm{St}^D_\Omega \approx 0.08$) could be found in a horizontal (zx)-plane inside the cavity flow. That means that both streamwise and spanwise velocity fluctuations – u' and w' – exhibit no variations at that frequency along the cavity span, suggesting a two-dimensional mode. Hence, the frequency f_Ω is not associated with centrifugal instabilities but rather confirms its connection with the shear layer flapping motion.

2. Broad-band peak f_Δ ($0.014 \leq St^D_\Delta \leq 0.024$)

The focus is now on the dynamical features of the modes associated with the broad-band peak centered around $\mathrm{St}^D_\Delta = f_\Delta D/U_0 \simeq 0.02$ and pointed out in Fig. 13. Such very low frequencies have been related to spanwise dynamics inside the cavity, independently of the shear layer flapping motion

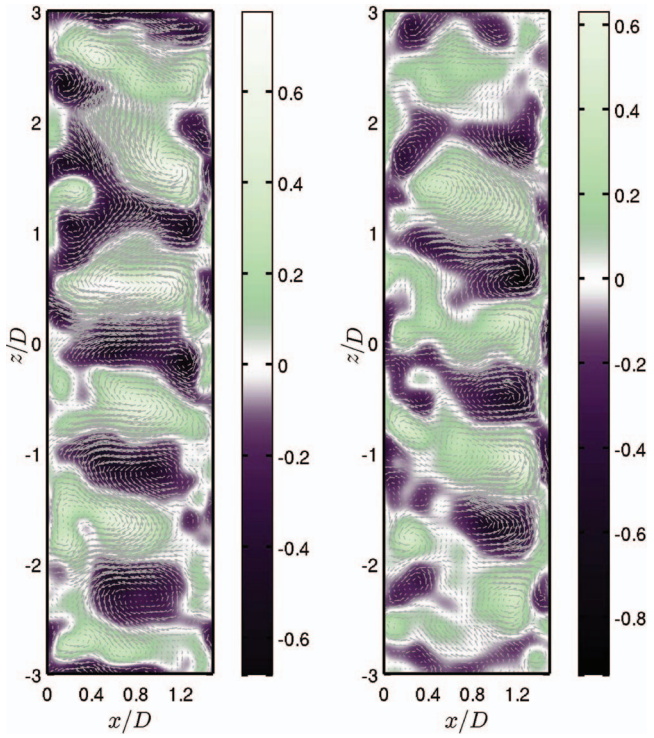

FIG. 15. Real part (left) and imaginary part (right) of the global Fourier mode $\mathbf{F}_\Delta(z, x)$, associated with the frequency $f_\Delta = 0.67$ Hz ($\mathrm{St}_\Delta^D = 0.016$) out of the broad-band peak.

(Neary and Stephanoff,[22] Faure *et al.*,[28,29] and Brès and Colonius[35]). In particular, numerical studies (Refs. 25, 31–35), in which the linear stability of a 2D base-flow has been investigated with regards to spanwise-traveling waves, have demonstrated that three-dimensional structures can arise due to centrifugal instabilities caused by the curvature of the main recirculation. Unstable eigenmodes are almost exclusively associated with dimensionless frequencies such that $\mathrm{St}^D < 0.03$.

The spatial structures shown in Figs. 14(c) and 14(d) depict the real and imaginary parts of a global Fourier mode associated with $\mathrm{St}_\Delta^D = 0.018$ ($f_\Delta = 0.77$ Hz), issued from the velocity fields in a xy-plane. The dynamics organizes primarily within the cavity, coiling up onto the main vortex. Fluctuations cover the entire inner-flow, where they outline the recirculation, especially in the outer-edges along the walls. That signature is sensibly consistent with the eigenmodes obtained by global stability analyses, see Refs. 32–35. However, this does not demonstrate unambiguously a three-dimensional organization of the inner-flow. Velocity fields in the spanwise horizontal (zx)-plane should give access to spanwise structures, would they actually exist.

Figure 15 shows the real and imaginary parts of the global Fourier mode, $\mathbf{F}_\Delta(z, x)$, associated with $\mathrm{St}_\Delta^D = 0.016$ ($f_\Delta = 0.67$ Hz), in the (zx)-plane located inside the cavity at $y/D = -1/3$. Spatial structures are displayed as observed from below.

Global Fourier mode $\mathbf{F}_\Delta(z, x)$ exhibits coherent structures, of alternate vorticity along the span, with a wavelength around $1.2\,D$. Note that spatial structures associated with other frequencies of the broad-band peak have been considered. They all depict similar spanwise waves with wavelengths varying around $\lambda_\Delta \approx D$. This matches the results of the global stability analyses showing the onset of such spanwise-traveling waves, see Refs. 25, 31–35.

As the present (experimental) study deals with the saturated regime, the dynamics depicted in Fig. 15 can also be seen as pairs of counter-rotating eddies distributed along the span and drifting laterally. Such an organization would be reminiscent of the Taylor-Görtler instabilities. Indeed, many references (Refs. 23–29) have reported Taylor-Görtler vortices being generated along the curvature of the main recirculation by centrifugal effects. As a result, the spanwise dynamics observed here

(Fig. 15) confirm that centrifugal instabilities continue to produce highly coherent structures at high Reynolds numbers despite the onset of shear layer instabilities.

In addition, the three-dimensional structures, saturated and disturbed by shear layer inflows, interact significantly with the flapping motion of the shear layer. In Fig. 7(a), the envelop of crosswise fluctuations v' indicates a drastic amplitude modulation of the self-sustained oscillations by the broad-banded dynamics of the inner-flow.

VII. CONCLUSIONS

The present study has brought more insight about the sources of amplitude modulations of the self-sustained oscillations in open cavity flows. It has been achieved through the experimental investigation of an incompressible multi-modulated flow, exhibiting several distinct low frequency dynamics. In order to characterize in detail the three-dimensional space-time organization of the flow in the permanent regime, time-resolved two-dimensional two-components velocity fields were acquired by PIV in both cross-stream and spanwise planes and stacked so as to access time-series everywhere in the region of interest. Such time-resolved space-extended datasets notably give access to the spatial structures associated with any frequency. These spatial structures, equivalently global Fourier modes or dynamic modes, provide insightful information about the coherent structures of the flow.

We have identified salient features commonly encountered in impinging shear flows: (i) *Kelvin-Helmholtz* waves are excited in the shear layer, as indicated by the non-dispersive properties and the spatial organization of the shear layer modes. (ii) The presence of the two cavity edges, responsible for an instantaneous feedback-loop based on pressure, causes the flow to become absolutely unstable: only a handful of *locked-on* modes are attainable and common to the entire flow. The corresponding frequencies are distributed such that $fL/U_0 \approx n/2$, $n = \{1, 2, 3\}$, as consistently reported in the literature. (iii) Depending on the control parameter L/θ_0, one or often several frequencies are selected and enhanced among the locked-on modes. *Carrier* frequencies are dominant and produce harmonics: they represent most of the self-sustained oscillations. They are usually accompanied with *side-band* frequencies, which convey the existence of amplitude modulations due to two-dimensional interactions at the impingement. The modulating frequencies f_b (for instance, $f_b = f_+ - f_a$), such that $0.25 \leq f_b L/U_0 \leq 0.4$, are here referred to as *edge frequencies*.

From time-resolved space-extended data, it was possible to better-understand the interactions between shear layer modes and inner-flow. Space-time structures have shown that amplitude modulations of the self-sustained oscillations are interlocked with *slow dynamics* inside the cavity. Indeed, the second source of amplitude modulations of the self-sustained oscillations comes from three-dimensional dynamics related to *centrifugal* effects around the main recirculation. However, the spanwise waves arising from centrifugal instabilities are generally observed and discussed for low control parameters before the onset of self-sustained oscillations in the impinging shear layer. In the present work, control parameters were much higher: namely, $\mathrm{Re}_L = 10200$ and $L/\theta_0 = 76$, which implied dramatic disturbances of the inner-flow by the shear layer. It is therefore most astonishing to find *spanwise waves* inside the cavity, highly coherent and powerful, recalling of the Taylor-Görtler vortices reported in the literature. The dynamics of the inner-flow cannot be fully restricted to a single scale. It yields a *continuum* of modes with spanwise wavelengths of the order of the cavity depth – $\lambda_\Delta \approx D$ – associated with *broad-banded* low frequencies such that $0.014 \leq f_\Delta D/U_0 \leq 0.024$. The space-time coherent structures reported here encompass most of the characteristic features of the inner-flow. In particular, spanwise traveling waves were found to influence drastically the self-sustained oscillations of the shear layer, both through amplitude modulation of the self-sustained oscillations and superimposition of the low frequency fluctuations of the inner-flow.

We also brought out another non-linear interaction between the shear layer and the inner-flow. For some cases reported in the parametric study, self-sustained oscillations are modulated in amplitude by three different frequencies. The narrow-peaked frequency f_Ω adds to the typical edge frequency f_b and the broad-banded frequency f_Δ deriving from centrifugal instabilities. In the configuration investigated here, the modulating frequency $f_\Omega L/U_0 = 0.12$ even overrides f_b and is responsible for the most salient amplitude modulation. The study has revealed that f_Ω does not

result from centrifugal instabilities, as its associated spatial structure is drastically different from the one associated with f_Δ. The frequency f_Ω has no signature in a spanwise (zx)-plane inside the cavity. In fact, the frequency f_Ω pertains to a *triadic* family with the dominant (f_a) and side-band $(f_\ell = f_a - f_\Omega)$ frequencies of the shear layer. The non-linear interaction between the modulating frequency and the two shear layer frequencies occurs at the impingement. However, the modulating frequency (f_Ω) might be preexisting to the side-band frequency (f_ℓ), contrarily to a standard edge frequency, since f_ℓ does not belong to locked-on modes. The reason for the appearance of such a low frequency f_Ω hence remains unclear. Nonetheless, we showed that f_Ω is associated with purely two-dimensional dynamics. It outlines inflows that carry momentum from the trailing edge to the bottom of the cavity *via* the recirculating flow. The slow dynamics near the bottom of the cavity are directly connected to the amplitude modulations of the shear layer oscillations. Furthermore, low frequencies f_Ω are only observed over a very restricted range of the control parameter *L/D*. This points out the predominant role played by the geometry of the cavity. Geometry-dependent dynamics revealing a two-dimensional connection between the shear layer and the internal flow suggests that the low frequency f_Ω be related to the recirculating flow inside the cavity.

ACKNOWLEDGMENTS

The authors want to acknowledge Christelle Douay for her contribution to the last PIV measurements. J.B. is grateful to Professor Julio Soria of Monash University for his support and advice. This work has been supported by Direction Generale de l'Armement and Agence Nationale de la Recherche (project ANR-06-BLAN-0363).

[1] R. W. Miksad, "Experiments on nonlinear stages of free shear layer transition," J. Fluid Mech. **56**, 695–719 (1972).
[2] R. W. Miksad, "Experiments on nonlinear interactions in the transition of a free shear layer," J. Fluid Mech. **59**, 1–21 (1973).
[3] A. Powell, "On edge tones and associated phenomena," Acustica **3**, 233–243 (1953).
[4] A. Powell, "On the edgetone," J. Acoust. Soc. Am. **33**, 395–409 (1961).
[5] J. E. Rossiter, "Wind-tunnel experiments on the flow over rectangular cavities at subsonic and transonic speeds," Aeronaut. Res. Counc. Rep. Memo. **3438** (1964).
[6] V. Sarohia, "Experimental investigation of oscillations in flows over shallow cavities," AIAA J. **15**, 984–991 (1977).
[7] D. Rockwell and E. Naudascher, "Self-sustained oscillations of impinging free shear layers," Annu. Rev. Fluid Mech. **11**, 67–94 (1979).
[8] C. K. Mamun and L. S. Tuckerman, "Asymmetry and Hopf bifurcation in spherical Couette flow," Phys. Fluids **7**, 80–91 (1995).
[9] D. Sipp and A. Lebedev, "Global stability of base and mean flows: A general approach and its applications to cylinder and open cavity flows," J. Fluid Mech. **593**, 333–358 (2007).
[10] D. Rockwell, "Prediction of oscillation frequencies for unstable flow past cavities," Trans. ASME: J. Fluids Eng. **99**, 294–300 (1977).
[11] D. Rockwell and E. Naudascher, "Review—Self-sustaining oscillations of flow past cavities," J. Fluids Eng. **100**, 152–165 (1978).
[12] C. Knisely and D. Rockwell, "Self-sustained low-frequency components in an impinging shear layer," J. Fluid Mech. **116**, 157–186 (1982).
[13] M. A. Kegerise, E. F. Spina, S. Garg, and L. N. Cattafesta III, "Mode-switching and nonlinear effects in compressible flow over a cavity," Phys. Fluids **16**, 678–687 (2004).
[14] N. Delprat, "Rossiter formula: A simple spectral model for a complex amplitude modulation process?," Phys. Fluids **18**, 071703 (2006).
[15] N. Delprat, "Low-frequency components and modulation processes in compressible cavity flows," J. Sound Vib. **329**, 4797–4809 (2010).
[16] L. R. Pastur, F. Lusseyran, T. M. Faure, Y. Fraigneau, R. Pethieu, and P. Debesse, "Quantifying the non-linear mode competition in the flow over an open cavity at medium reynolds number," Exp. Fluids **44**, 597–608 (2008).
[17] F. Lusseyran, L. R. Pastur, and C. Letellier, "Dynamical analysis of an intermittency in an open cavity flow," Phys. Fluids **20**, 114101 (2008).
[18] D. Rockwell and C. Knisely, "Vortex edge interaction: Mechanisms for generating low frequency components," Phys. Fluids **23**, 239–240 (1980).
[19] J. Malone, M. Debiasi, J. Little, and M. Samimy, "Analysis of the spectral relationships of cavity tones in subsonic resonant cavity flows," Phys. Fluids **21**, 055103 (2009).
[20] D. Rockwell and C. Knisely, "Observations of the three-dimensional nature of unstable flow past a cavity," Phys. Fluids **23**, 425–431 (1980).
[21] J. R. Koseff and R. L. Street, "Visualization studies of a shear driven three-dimensional recirculating flow," Trans. ASME: J. Fluids Eng. **106**, 21–29 (1984).

[22] M. D. Neary and K. D. Stephanoff, "Shear-layer-driven transition in a rectangular cavity," Phys. Fluids **30**, 2936–2946 (1987).
[23] S. Albensoeder, H. C. Kuhlmann, and H. J. Rath, "Three-dimensional centrifugal-flow instabilities in the lid-driven-cavity problem," Phys. Fluids **13**, 121–135 (2001).
[24] S. Albensoeder and H. C. Kuhlmann, "Accurate three-dimensional lid-driven cavity flow," J. Comput. Phys. **206**, 536–558 (2005).
[25] S. Albensoeder and H. C. Kuhlmann, "Nonlinear three-dimensional flow in the lid-driven square cavity," J. Fluid Mech. **569**, 465–480 (2006).
[26] J.-L. Guermond, C. Migeon, G. Pineau, and L. Quartapelle, "Start-up flows in a three-dimensional rectangular driven cavity of aspect ratio 1:1:2 at re = 1000," J. Fluid Mech. **450**, 169–199 (2002).
[27] C. Migeon, G. Pineau, and A. Texier, "Three-dimensionality development inside standard parallelepipedic lid-driven cavities at re = 1000," J. Fluids Struct. **17**, 717–738 (2003).
[28] T. M. Faure, P. Adrianos, F. Lusseyran, and L. R. Pastur, "Visualizations of the flow inside an open cavity at medium range Reynolds numbers," Exp. Fluids **42**, 169–184 (2007).
[29] T. M. Faure, L. R. Pastur, F. Lusseyran, Y. Fraigneau, and D. Bisch, "Three-dimensional centrifugal instabilities development inside a parallelepipedic open cavity of various shape," Exp. Fluids **47**, 395–410 (2009).
[30] V. Theofilis, "Advances in global linear instability of nonparallel and three-dimensional flows," Prog. Aerosp. Sci. **39**, 249–315 (2003).
[31] V. Theofilis and T. Colonius, "An algorithm for the recovery of 2- and 3-D BiGlobal instabilities of compressible flow over 2-d open cavities," AIAA Paper No. 2003–4143, 2003.
[32] J. de Vicente, "Spectral multi-domain method for the global instability analysis of complex cavity flows," Ph.D. thesis, Universidad Politécnica de Madrid, 2010.
[33] J. de Vicente, D. Rodriguez, V. Theofilis, and E. Valero, "Stability analysis in spanwise-periodic double-sided lid-driven cavity flows with complex cross-sectional profiles," Comput. Fluids **43**, 143–153 (2011).
[34] F. Meseguer-Garrido, J. de Vicente, E. Valero, and V. Theofilis, "Effect of aspect ratio on the three-dimensional global instability analysis of incompressible open cavity flows," in *Proceedings of the 6th AIAA Theoretical Fluid Mechanics Conference (TFMC6)*, Honolulu, HI, June 2011.
[35] G. A. Brès and T. Colonius, "Three-dimensional instabilities in compressible flow over open cavities," J. Fluid Mech. **599**, 309–339 (2008).
[36] X. Gloerfelt, "Compressible proper orthogonal decomposition/galerkin reduced-order model of self-sustained oscillations in a cavity," Phys. Fluids **20**, 115105 (2008).
[37] J. Basley, L. R. Pastur, F. Lusseyran, T. M. Faure, and N. Delprat, "Experimental investigation of global structures in an incompressible cavity flow using time-resolved PIV," Exp. Fluids **50**, 905–918 (2011).
[38] J. Basley, "An experimental investigation on waves and coherent structures in a three-dimensional open cavity flow," Ph.D. thesis, Université Paris-Sud Monash University, 2012.
[39] C. W. Rowley, T. Colonius, and A. J. Basu, "On self-sustained oscillations in two-dimensional compressible flow over rectangular cavities," J. Fluid Mech. **455**, 315–346 (2002).
[40] K.-M. Chung, "Three-dimensional effect on transonic rectangular cavity flows," Exp. Fluids **30**, 531–536 (2001).
[41] N. Forestier, L. Jacquin, and P. Geffroy, "The mixing layer over a deep cavity at high-subsonic speed," J. Fluid Mech. **475**, 101–145 (2003).
[42] L. Larchevêque, P. Sagaut, T. H. Lê, and P. Comte, "Large-eddy simulations of a compressible flow in a 3D open cavity at high Reynolds number," J. Fluid Mech. **516**, 265–301 (2004).
[43] G. M. Quénot, J. Pakleza, and T. A. Kowalewski, "Particle image velocimetry with optical flow," Exp. Fluids **25**, 177–189 (1998).
[44] M. Stanislas, M. Okamoto, C. J. Kähler, and J. Westerweel, "2nd international PIV challenge," Exp. Fluids **39**, 170–191 (2005).
[45] M. Stanislas, K. Okamoto, C. J. Kähler, J. Westerweel, and F. Scarano, "Main results of the third international PIV challenge," Exp. Fluids **45**, 27–71 (2008).
[46] X. Gloerfelt, C. Bogey, and C. Bailly, "Numerical evidence of mode switching in the flow-induced oscillations by a cavity," Int. J. Aeroacoust. **2**, 193 (2003).
[47] D. R. Williams and F. R. Hama, "Streaklines in a shear layer perturbed by two waves," Phys. Fluids **23**, 442–447 (1980).
[48] C.-H. Kuo and S.-H. Huang, "Influence of flow path modification on oscillation of cavity shear layer," Exp. Fluids **31**, 162–178 (2001).
[49] P. A. Monkewitz and P. Huerre, "Influence of the velocity ratio on the spatial instability of mixing layers," Phys. Fluids **25**, 1137–1143 (1982).
[50] A. Michalke, "On the inviscid instability of the hyperbolic tangent velocity profile," J. Fluid Mech. **19**, 543–556 (1964).
[51] A. Michalke, "On spatially growing disturbances in a shear layer," J. Fluid Mech. **23**, 521–544 (1965).
[52] P. Huerre and M. Rossi, *Hydrodynamics and Nonlinear Instabilities* (Cambridge University Press, Cambridge, England, 1998), Chap. II, pp. 81–294.
[53] D. Rockwell, "Oscillations of impinging shear layers," AIAA J. **21**, 645–664 (1983).
[54] P. J. Schmid, "Dynamic mode decomposition of numerical and experimental data," J. Fluid Mech. **54**, 5–28 (2010).
[55] C. W. Rowley, I. Mezić, S. Bagheri, P. Schlatter, and D. S. Henningson, "Spectral analysis of nonlinear flows," J. Fluid Mech. **641**, 115–127 (2009).
[56] D. Duke, J. Soria, and D. Honnery, "An error analysis of the dynamic mode decomposition," Exp. Fluids **52**, 529–542 (2012).
[57] D. Duke, D. Honnery, and J. Soria, "Experimental investigation of nonlinear instabilities in annular liquid sheets," J. Fluid Mech. **691**, 594–604 (2012).